Invited Research article

Low-angle eolian deposits formed by protodune migration, and insights into slipface development at White Sands Dune Field, New Mexico

J.D. Phillips[a], R.C. Ewing[a,*], R. Bowling[a], B.A. Weymer[b], P. Barrineau[c], J.A. Nittrouer[d], M.E. Everett[a]

[a] Texas A&M University, Department of Geology and Geophysics, College Station, TX 77843, United States
[b] GEOMAR – Helmholtz Centre for Ocean Research Kiel, Wischhofstraße 1-3, 24148 Kiel, Germany
[c] Texas A&M University, Department of Geography, College Station, TX 77843, United States
[d] Rice University, Department of Earth, Environmental and Planetary Sciences, Houston, TX, United States

ARTICLE INFO

ABSTRACT

Protodunes emerge from a flat sand bed at the upwind margin of White Sands Dune Field, and, over several hundred meters, transition into fully developed dunes. Here, we investigate spatial and temporal changes in topography across this transition from 2007 to 2016 using lidar-derived topography, structure-from-motion-derived topography, and RTK GPS. We characterize the deposits present in 2015 using ground penetrating radar. Symmetric protodunes give way downwind to an asymmetric protodune at the transition to slipface development. Between 2007 and 2016, protodune amplitude increased from 0.2 m to 4.0 m, migration rate increased from 3.2 m/yr to 6.1 m/yr, and wavelength increased from 76 m to 122 m. Ground-penetrating radar surveys show strata between flat and 15° make up the stratigraphic architecture of the protodunes. Strata increase in steepness commensurate with an increase in amplitude. Decimeter accumulations of low-angle strata associated with initial protodune stages give way to 4 m of accumulation composed of sets up to 1 m thick prior to slipface development. Topsets present in the thickest sets indicate near critical angles of bedform climb. Growth and slipface development occur by aerodynamic sand trapping and protodune merging. Changes in asymmetry erase initial slipfaces prior to permanent slipface development, after which efficient sand trapping and scour promotes the transition to a dune across 20 m in 5 years. Protodune stratification has hallmarks of sandsheet stratification and can be appreciated within the greater suite of processes that create low-angle eolian stratification found in modern and ancient environments.

1. Introduction

Low-angle eolian deposits occur as a transitional facies at the edges of modern dune fields and in ancient successions (Fryberger et al., 1979; Loope, 1984, 1985; Kocurek and Nielson, 1986; Chan and Kocurek, 1988; Chan, 1989; Mountney, 2006; Jordan and Mountney, 2010). Typically, low-angle eolian deposits compose sandsheets characterized by low-relief topography, vegetation, and poorly sorted sand (Fryberger et al., 1979; Kocurek and Nielson, 1986). As a transitional facies, low-angle deposits are thought to form where high-angle dune deposits cannot, due to, for example, vegetation, abundant coarse grains, a shallow water-table, periodic flooding, and surface cementation (e.g., Fryberger et al., 1979; Kocurek and Nielson, 1986). Sandsheets, however, also develop during the initial phase of dune growth, independent of factors preventing dune formation. This initial phase of

dune growth is manifested by protodunes (e.g., Kocurek et al., 1992).

Protodunes are transient, low-relief, slipfaceless bedforms that form prior to mature sand dunes (i.e., dunes that have an angle-of-repose slipface) (Fig. 1) (Cooper, 1958; Kocurek et al., 1992; Lancaster, 1996; Momiji et al., 2002, Andreotti et al., 2010; Elbelrhiti, 2012, Nield et al., 2011; Kocurek and Ewing, 2016). That protodunes are low-relief, slipfaceless bedforms that form independent of factors preventing dune formation, raises a question concerning the role protodune migration plays in the development of low-angle deposits. Put another way, rather than low-angle deposits arising due to the prevention of dune formation (i.e., Kocurek and Nielson, 1986), could some low-angle deposits represent protodune growth and migration? This lends to the hypothesis that low-angle deposits are a necessary precursor to dune deposits, which begs the question: How do low-angle deposits transition to angle-of-repose dune deposits?
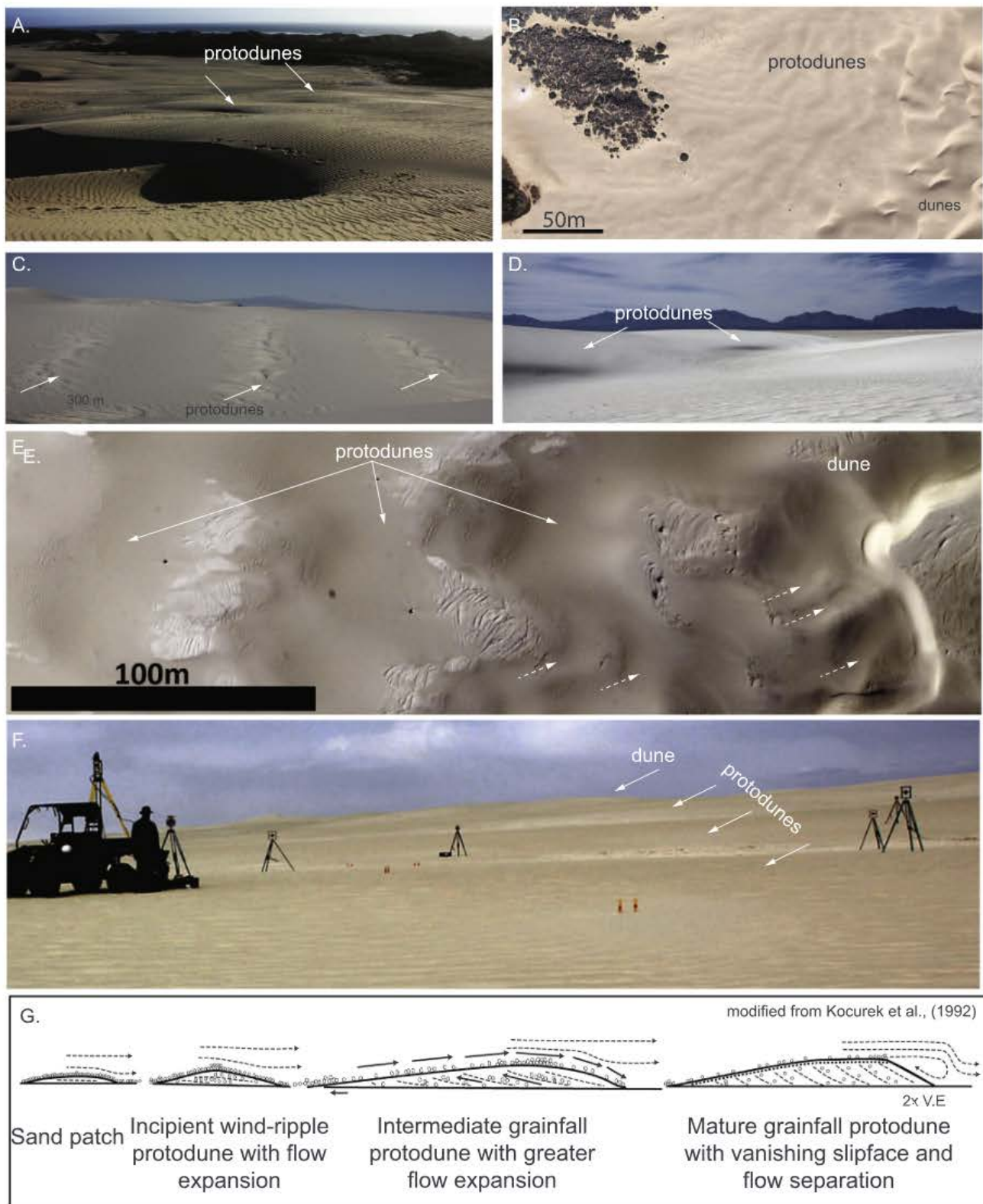

Fig. 1. Images of protodunes. Solid white arrows point to the crests of the protodunes. (A) Train of protodunes at the upwind margin of Oceano, Dunes, CA, USA. (B) Google Earth satellite image of protodunes at the upwind margin of Oceano Dunes. (C) Protodunes on the stoss slope of a dune at White Sands Dune Field, NM, USA. (D) Mature protodunes at the upwind margin of White Sands Dune Field. (E) 2012 aerial image of the protodune-to-dune transition at the upwind margin of White Sands. The bright inter-protodune areas contain dune cross-stratification. The brightness on the protodunes approximately corresponds to protodune steepness and grain size. Coarse grains mantle the stoss slopes and create a darker appearance. Finer grains cover the lee sides, which also become progressively steeper and brighter toward the first dune. Note the smaller protodunes forming on the flanks of the larger protodunes indicated by the dashed white arrows. Coarse grained ripples are visible on the stoss slope of the protodunes. The image is not of the study area. (F) Photo taken looking toward the first dune across three protodunes near the study area at White Sands Dune Field. Note the sediment free inter protodune areas and coarse-grained ripples on the protodune surface. (G) Model of protodune formation modified from Kocurek et al. (1992).

This study links protodune morphodynamics with the development of low-angle deposits and assesses the morphologic and stratigraphic transition from protodunes to dunes. Herein, observations from the upwind margin at White Sands Dune Field, New Mexico, USA, are used to examine the (1) spatial and temporal changes in protodune morphology, (2) deposits formed by migrating protodunes, and (3) morphology and stratigraphy formed by protodunes transitioning to mature dunes.

1.1. Protodunes

Protodunes are included within a class of slipfaceless bedforms described as sandy hummocks, heaps, elementary dunes, dome dunes, whaleback dunes, and zibars (Holm, 1960; Warren, 1971; Wilson, 1973; Lancaster, 1982; Nielson and Kocurek, 1986; Bristow et al., 2010; Kroy et al., 2002; Elbelrhiti et al., 2005). Classifications of these types of bedforms have been discerned based on morphology (e.g., whaleback dunes), and boundary conditions that affect the morphology such as grain size (e.g., zibar) and sediment availability (e.g., dome dune). These bedforms, however, are linked by process as protodunes because they are dune-scale emergent bedforms that could eventually develop into fully mature dunes limited only by the boundary conditions within which they form (e.g., grain size for zibars) (e.g., Andreotti et al., 2010).

The temporal transition of protodunes from a flat bed of sand into low-relief bedforms and, eventually mature dunes, has been observed in coastal settings where seasonal reworking of dune systems results in the annual regrowth of a dune field (Cooper, 1958; Kocurek et al., 1992), in barchan dune systems (Elbelrhiti et al., 2005; Elbelrhiti, 2012), and in landscape-scale experiments where dunes that were removed subsequently regrew (Elbelrhiti et al., 2005; Ping et al., 2014). Nield et al. (2011) documented a wet-to-dry transition on a beach, in which sand strips and protodunes developed where the beach dried and sand availability increased. Baddock et al. (2018) documented vertical growth of protodunes in a matter of hours, and established the feedbacks between the flow and the evolving forms that drive protodune morphodynamics. These include the erosion-deposition transition occurring upwind of the crest, and the transition to a steeper lee and more gently sloping stoss slope.

In their seminal study at Padre Island, Texas, Kocurek et al. (1992) documented the temporal transition from protodunes to dunes over the course of a wet-to-dry seasonal change, whereby sand initially accumulates as patches, then transitions to low-angle wind-rippled-to-grainfall protodunes, before developing into mature dunes (Fig. 1f). An increase in protodune amplitude and concomitant steepening of the lee slope characterizes the protodune-to-dune transition. Airflow over the bedform develops from flow-attached to flow-separated (Fig. 1). Kocurek et al. (1992) also noted that wind ripples form on the lee slopes with angles less than 10°, and grainfall forms at the lee slope at angles between 10° and 34°. Grainflows develop as the lee slope steepened to the angle of initial yield.

Kocurek et al. (1992) attributed the stability of the protodunes greater than ~10 m to the length over which the wind transitioned from undersaturated to saturated, as noted by Bagnold (1941). Based upon older fluvial studies (e.g., Smith, 1970; Richards 1980), recent eolian theoretical studies, experiments, and field observations establish quantitative measures of the fluid dynamic and sand transport controls on protodune initiation, stability, and growth (Sauermann et al., 2001; Andreotti et al., 2002, 2010; Elbelrhiti et al., 2005; Charru, 2006; Fourriere et al., 2010). A shift in the maximum shear stress to upwind of the crest (e.g., Jackson and Hunt, 1975; Claudin et al., 2013), and a spatial lag in sand transport that occurs with changes in shear stress (e.g., the saturation length of Hersen et al., 2002; Andreotti et al., 2010) are thought to be requirements for protodune growth. Various physical mechanisms could account for the saturation length (see review in Andreotti et al., 2010; Durán et al., 2011), but the so-called drag length

is a simple formulation that suggests that grain inertia scales with grain size and fluid density, which correlate to protodune size (e.g., Hersen et al., 2002; Claudin and Andreotti, 2006; Andreotti et al., 2010).

The spatial transition from protodunes to mature dunes is not as well documented as the temporal transition, but such a transition should occur where any point or line source of sediment provides sediment input downwind to a dune field (e.g., Elbelrhiti et al., 2005; Ewing and Kocurek, 2010; Eastwood et al., 2011; Ewing et al., 2015; Kocurek and Ewing, 2016). Protodunes transitioning to mature dunes on the stoss slope of a barchan dune (Fig. 1C) (Elbelrhiti et al., 2005), and transitioning to mature dunes at the upwind margin of dune fields (Fig. 1 A, B, D, F) (Ewing et al., 2015) exemplify this spatial transition. Advantageously, at any given time, point- and line-sourced dune-field margins typically display all stages of protodune growth and the transition to mature dunes.

The upwind margin of the White Sands Dune Field provides an ideal setting to examine all stages of the transition of protodunes into mature dunes in a line-sourced setting. Multi-temporal topography datasets afford the opportunity to examine both spatial and temporal changes in protodunes. Additionally, the wide grain size distribution that characterizes this setting affords an opportunity to evaluate the relationship between protodune size and grain size within the context of the flux saturation length scale (e.g. Hersen et al., 2002).

2. Geologic background

White Sands Dune Field (Fig. 2) covers nearly 500 km² of the Tularosa Basin in southern New Mexico. The Tularosa Basin is a north-south trending fault-bounded graben formed at the eastern extent of the Basin and Range Tectonic Province and within the Tertiary Rio Grande Rift (McKee, 1966; Seager and Morgan, 1979; Langford, 2003; Kocurek et al., 2007). The San Andres and Sacramento Mountains flank the basin to the west and east, respectively. The mountains consist of Paleozoic carbonate and evaporite units, and provide alluvial fill to the basin. The carbonate and evaporite basin fill, along with the restricted groundwater outflow, gives rise to a recent stratigraphic history dominated by lacustrine and playa evaporitic environments. These environments have contributed substantially to the formation of the modern gypsum dune field (Fryberger, 2001; Langford, 2003; Kocurek et al., 2007; Baitis et al., 2014).

The most recent basin-scale lake, Pleistocene Lake Otero, occupied the western part of the basin during the Last Glacial Maximum (Langford, 2003; Allen et al., 2009). During Early to Mid-Holocene, progressive drying and eolian deflation coincided with the retreat of lake. Deflation of lake strata supplied sediment and contributed to the morphology of the modern dune field (Langford, 2003; Kocurek et al., 2007; Baitis et al., 2014). Today, the area previously occupied by Lake Otero hosts modern playa lakes, Alkali Flat - a large deflation plain, which lies directly west of the dune field, and the dune field.

Within the dune field, ENE dune migration occurs at an average rate of 3.6 m/yr driven dominantly by springtime winds out of the SW (Fryberger, 2001; Jerolmack et al., 2011; Pedersen et al., 2015). Lesser winds out of the NNW during the winter and SSE throughout the year moderately affect the shape and migration direction of the dunes (Pedersen et al., 2015; Swanson et al., 2016). Beyond the transition from barchanoid dunes into vegetated parabolic dunes, the dune field terminates into a loess-dominated silty sand sheet that interfingers with alluvial fans shed from the Sacramento Mountains (Mckee, 1966; Seager et al., 1987; Newton and Allen, 2014).

Herein, this study focuses on the upwind dune field margin at the eastern edge of Alkali Flat. Sediment influx to the margin derives from deflation of gypsiferous paleolake strata and gypsum produced by active playas (Fig. 3). These sediment sources create a line source of sediment influx to the dune field, which facilitates the formation of a low-relief sand ramp (Fryberger, 2001; Ewing and Kocurek, 2010, Jerolmack et al., 2012). The sand ramp defines the transition between
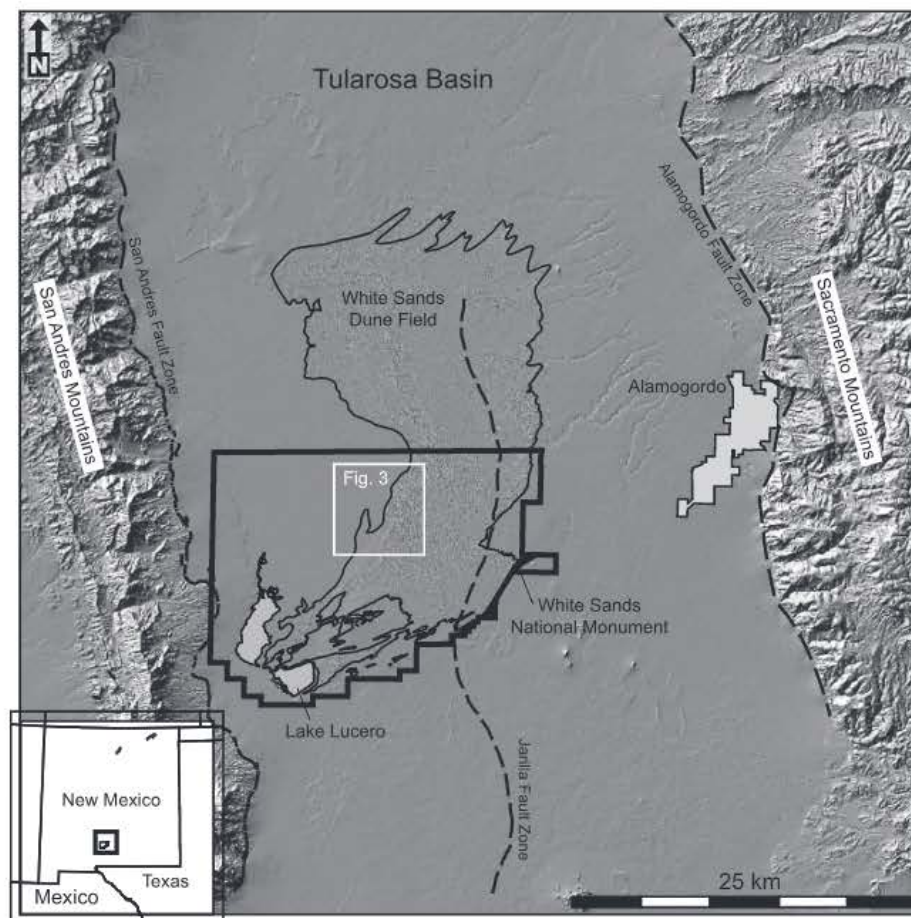
Fig. 2. Location of White Sands Dune Field in southern New Mexico, USA. Radar derived topographic hillshade represents the topography of the Tularosa Basin. The thin and bold black outlines highlight White Sands Dune Field and White Sands National Monument, respectively.

Alkali Flat and the dune field (Fig. 4). Across the sand ramp, protodunes form and transition downwind into mature dunes that mark the beginning of the dune field (Fig. 4).

3. Methods

Digital elevation models (DEMs), ground-penetrating radar (GPR), RTK (real-time kinematic) GPS, and sediment samples were used to investigate the morphology, internal stratigraphy, and grain size over the protodune-to-dune transition at the upwind margin. DEMs derived from airborne lidar from 2007, 2008, 2009, 2010, and 2015, and structure-from-motion photogrammetry from 2016 were used to evaluate the geomorphic evolution of the sand ramp through time. Topographic profiles were extracted using GIS. Because the topographic data sets were collected with different vertical datums, all elevations were collapsed to the same point at the upwind start of the transect to generate common reference elevations along spatially co-registered transects.

A 784-m-long GPR/GPS transect oriented at 075° azimuth was collected at the upwind margin of the dune field (Figs. 3 and 4). The transect was aligned approximately parallel with the primary, south-westerly (065°) winds and was aligned orthogonal to the dominant dune crestline orientation between 315° and 345° (Ewing et al., 2006, Rachal and Dugas, 2009; Baitis et al., 2014). The GPR data were collected with a sled mounted, 200 MHz pulseEKKO Pro GPR system manufactured by Sensors and Software. The GPR was operated in a bistatic collection mode, wherein a signal is transmitted by one dipole antenna and received by a parallel dipole antenna separated by 0.5 m along the sled. Radar traces were collected at 0.1 m intervals along a

measuring tape, which is well below the minimum sampling rate of 0.2 m for antennas with a 200 MHz center frequency as required by the Nyquist sampling theorem (Annan, 2009). This sampling interval ensures no spatial aliasing occurs from under-sampled subsurface features (Bristow, 2009).

Topographic measurements were collected independently from the GPR survey along the transect starting from Alkali Flat and progressing downwind to past the first distinguishable dune slipface and onto the adjacent stoss slope. Topographic measurements were collected with a spacing distance of 0.1 m (measured along the tape measure); this distance coincided best with the GPR step size, and was sufficient for capturing high-resolution measurements of slope breaks (i.e., areas with high topographic variation). The topographic survey utilized differential GNSS measurements and incorporated RTK corrections broadcast from a stationary base station to the mobile rover unit. Horizontal and vertical errors were less than 0.003 m and 0.01 m, respectively. The topographic data were smoothed using a 3-point window smoothing filter, iterated four times, and then interpolated to a spacing of 0.1 m, to coincide with the GPR survey step size.

To produce an image appropriate for interpretation, de-wow, background subtraction, and a band-pass filter were applied to the raw GPR dataset. These processing steps removed DC bias and low-frequency inductive effects, unwanted sub-horizontal reflections, direct air-wave and ground-wave arrivals, signal ringing within the receiving antenna, and artifacts characterized by frequency content lying outside the bandwidth of the 200 MHz antennas (Annan, 2003). Fig. 5B exemplifies the effects of these processing steps. After filtering, a static topographic correction using the spline-interpolated GPS measurements translated each trace along the time-axis so that the first arrival of each
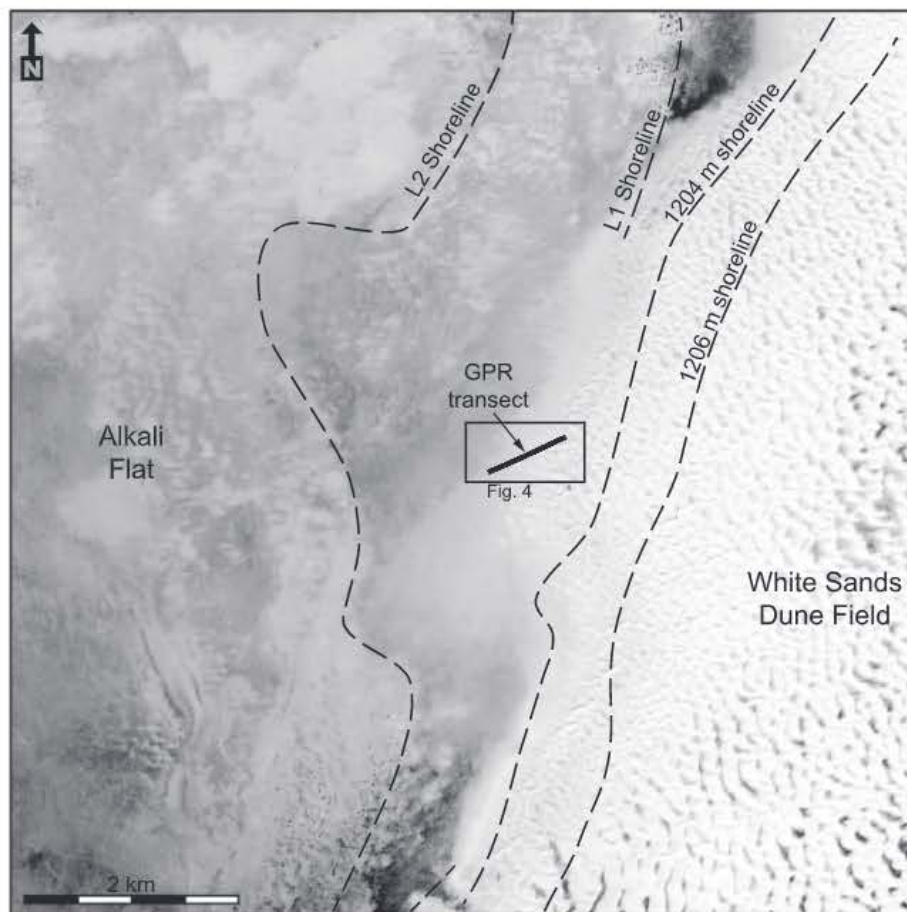
Fig. 3. Satellite image of the upwind margin of White Sands Dune Field. Alkali Flat deflation plain occupies the dark-toned areas to the west of the bright, white dune field. The GPR transect (bold black line) is located at the transitional zone between Alkali Flat and the dune field. Paleoshorelines of Pleistocene Lake Otero show previous locations of the lake (Langford, 2003; Baitis et al., 2014).

trace is positioned at its correct elevation along the survey line (Fig. 5C). Using trial values of dielectric constants between 5 and 10 (Young and Frederikse, 1973), a 0.122 m/ns subsurface velocity was empirically derived. When used in migration, this velocity was found to best collapse observed diffraction hyperbolae and allowed dipping reflections to be correctly oriented (Clarbout, 1985). This velocity was also used to convert two-way travel time to depth and gives a computed vertical resolution of 0.15 m, which agrees with the theoretical resolution for a 200 MHz survey in damp sand, as described by Jol and Bristow (2003). Automatic Gain Control amplified each recorded trace relative to a user defined maximum value (Yilmaz, 2001). This procedure eliminates relative amplitude variations within each trace, but highlights every reflector equably regardless of its burial depth. This is desirable for stratigraphic delineation and interpretation.

The processed GPR data were converted to SEG-Y format, which is standard in the near-surface geophysical exploration community for interpretation using Petrel software (Schlumberger). First-order bounding surfaces were identified within the data based on definitions by Brookfield (1977) and Kocurek (1991), as well as radar facies (Bristow et al., 2000; Jol and Bristow, 2003; Neal, 2004; Jol, 2009). From the interpreted stratigraphic packages, trends in apparent dip angle were easily observable and measured to assess the stratigraphic development along the surveyed transect.

Throughout the processed GPR profile, irregular radar reflections exist that resemble downward expanding, stacked semi-circles (Fig. 5C). Pre-migration, these data artifacts are anomalous radar return values recorded by the receiving antenna, which are displayed as points (Fig. 5B) and later 'smeared' into diffraction hyperbolae during migration (Fig. 5C). Although these values are almost insignificant in their initial radar amplitude returns (Fig. 5A), the gaining processes applies approximately equivalent amplitude values to all the recorded

measurements, resulting in an anomalously high amplitude appearance. For this reason, a mute was applied to later travel times along the transect to eliminate the artifacts below the depth where stratigraphy could be confidently interpreted (i.e., depth of investigation). The original anomalous reflections most likely are erroneous data artifacts recorded from the radio wave frequencies used in simultaneous RTK GNSS topographic surveying, and modified in the migration and gaining processes. However, due to the proximity of testing at the White Sands Missile Range, anomalous reflections occurring from buried unexploded ordinance or other metallic objects cannot be ruled out as contributing to some data artifacts.

Grain samples were collected in the field by scooping ~ 100 g from the surface and at 50 cm below the surface. Samples were analyzed using a Retsch Camsizer particle shape and size analyzer, which for each ~ 100 g sample measures hundreds of thousands of particles.

4. Results

4.1. Upwind margin morphology and sediment size

A sand ramp characterizes the upwind margin of the White Sands Dune Field where the landscape transitions from the sand-bare, deflationary hardpan of Alkali Flat, to sand patches, then protodunes, and ultimately mature dunes. The length of this transition is variable along the margin of the dune field, but at the study site the transition occurs over ~ 700 m with a commensurate rise in elevation of ~ 11 m (Fig. 4).

Dune-scale cross-stratification composes much of the hardpan floor of Alkali Flat near the sand ramp, and some surfaces between protodunes along the sand ramp (Figs. 1 and 4). Sand patches form in the lee of plants, behind low-relief topography generated by deflation of salt crusts, with minimal playa topography (i.e., cm-scale), and also with no
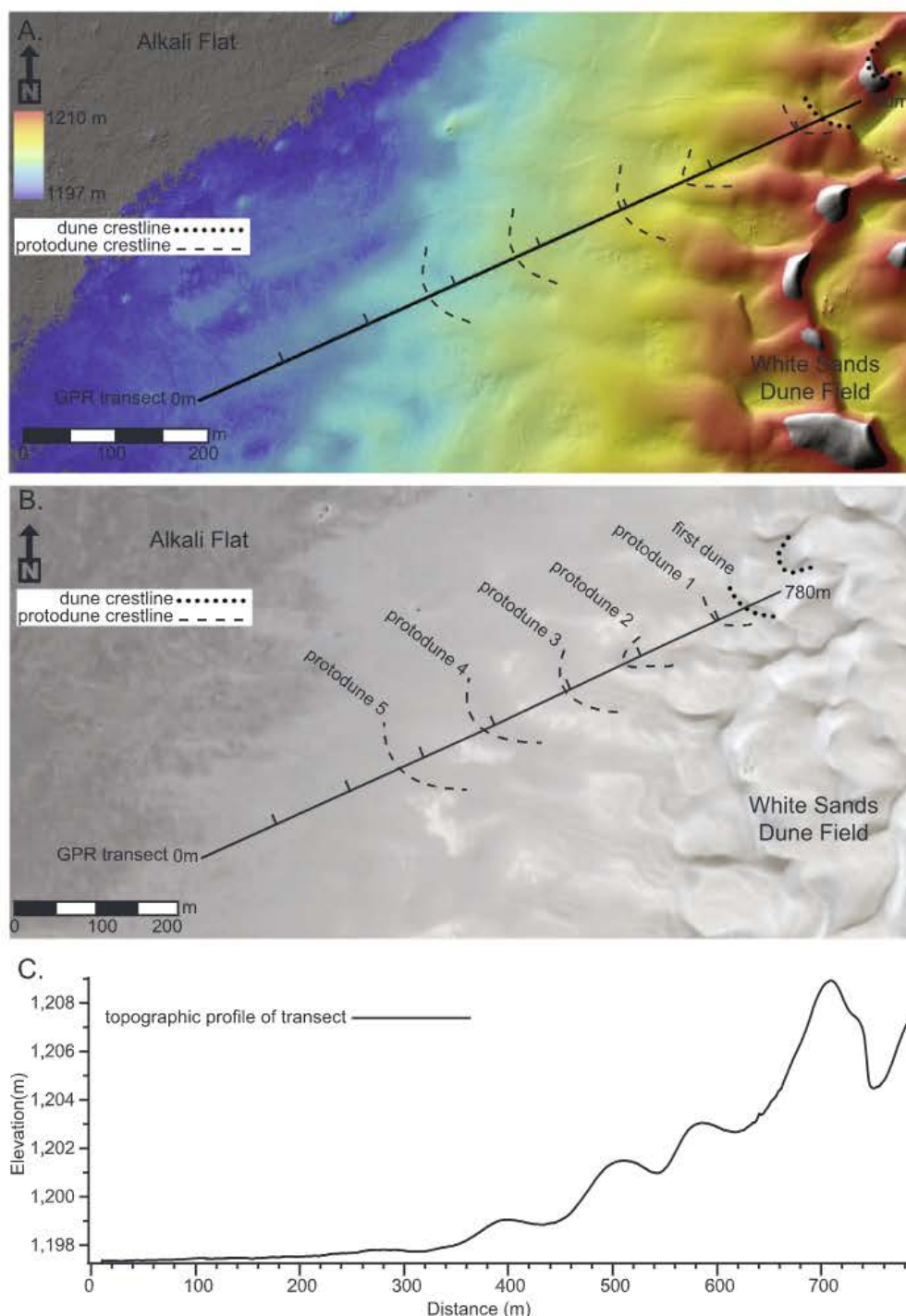
Fig. 4. Morphology of the upwind margin at White Sands. (A) August 2015 airborne lidar-derived topography shows 13 m of elevation change from Alkali Flat to the first dune. The GPR transect is shown as a solid black line marked with 100 m increments. Protodune and dune crestlines are highlighted by dashed (protodune) and stippled (dune) lines. (B) August 2015 satellite image showing the geomorphology of the margin. Protodunes and first dune are labeled and protodune and dune crestlines highlighted. (C) Topographic profile derived from the RTK GPS topography acquired during the November 2015 GPR field campaign. Note the increasing amplitude of the protodunes along the transect and the abrupt increase in amplitude of the last protodune, which becomes a dune.

apparent reliance on topography. Overall, sand cover increases toward the NE in the resultant transport direction, and eventually impact ripples, coarse-grained ripples, and lag deposits uniformly cover Alkali Flat.

As sand cover increases toward the NE along the sand ramp, undulating long wavelength- (i.e., decameter) and low amplitude- (i.e., centimeter) scale topography emerges from the otherwise flat landscape (Fig. 4). Protodunes are this topography. Crest-to-crest wavelengths from upwind (protodune 5 in Fig. 4C) to downwind (protodune 1 in Fig. 4C) are 134 m, 105 m, 71 m, and 128 m. Protodune lengths (stoss-to-lee) from upwind to downwind are 76 m, 76 m, 80 m, 88 m, 122 m. The amplitudes from upwind to downwind are 0.2 m, 0.4 m, 0.9 m, 0.9 m, and 4.0 m, respectively. The shapes of the protodunes vary across

the transect (Figs. 4 and 7). The shapes of the initial four protodunes (protodunes 5–2) are symmetric to slightly asymmetric, where the steepest slopes face the SW and into the dominant wind direction. The shape of the last protodune is asymmetric, where the steepest slope faces NE.

Surface samples have a median grain size (d50) of 0.67 mm ($n = 9$), and a maximum grain size of 1.0 mm. Grain samples collected ~50 cm below the surface have a d50 of 0.23 mm, and a maximum size of 0.88 mm ($n = 9$). A > 1 mm size fraction sparsely populates the surface (Fig. 6). The coarse sand and > 1 mm size fraction composes patches of coarse-grained ripples regularly spaced with patches of impact ripples composed of medium sand. Progressing gradationally downwind, the coarse-grained ripple patches superpose well-defined protodunes. The
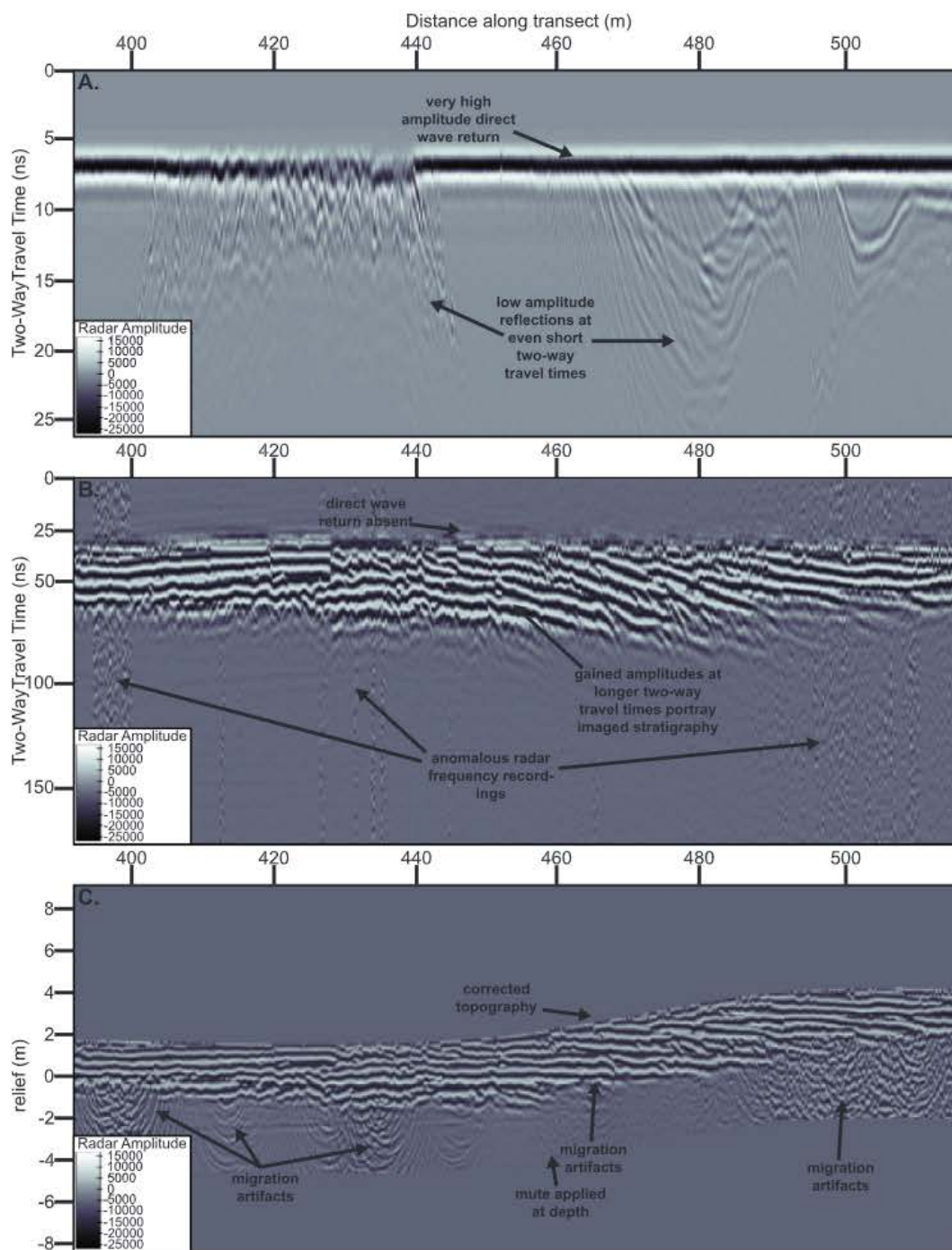
Fig. 5. Images of GPR data processing method. Example from central portion of transect (A) Raw GPR data. (B) Data after de-wow, background subtraction, and band-pass filtering applied. AGC gain applied for display. (C) Final GPR image after topographic correction and migration. AGC gain applied for display. Mute applied to eliminate artifacts existing significantly below the depth of investigation.

patches distribute across the protodunes such that coarse-grained ripples concentrate upwind of the crests and impact ripples concentrate leeward of the crests. The medium sand size fraction occurs as grainfall on high-relief protodunes, as noted by a smooth and featureless (i.e., no impact ripples are present) surface and in the lee of the first mature dune. Shallow trenching revealed planar, parallel, 'pin-stripe' lamination in the subsurface of a protodune crest (Fig. 6). Given the coarseness of the upwind margin and the size of the protodunes, Kocurek and Ewing (2016) described these features as proto-zibars, but they are herein referred to as protodunes based on the process classification as emergent dune-scale bedforms.

4.2. Changes across the upwind margin between 2007 and 2016

Translating and deforming sand patches and protodunes changed the sand ramp topography between 2007 and 2016. Sand patches emerging at the SW edge of the transect have irregular shapes that decorrelate between years, which prevented measurements of sand patch migration (Fig. 12A). In contrast, the well-defined protodune shape correlates between years such that migration could be measured. The protodunes migrate at steadily increasing rates to the NE. The nine-year average migration rates of the protodunes from the most upwind protodune (i.e., protodune 5) to the last, downwind protodune (i.e.,
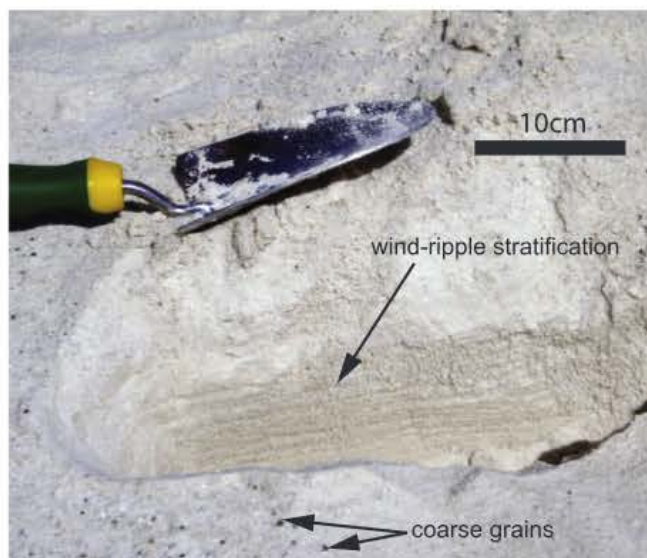
Fig. 6. Trench into a protodune showing wind ripple lamination. Coarse-grained lag at the surface noted by black arrows.

protodune 1) are 3.2 myr^{-1}, 4.7 myr^{-1}, 4.5 myr^{-1}, 6.1 myr^{-1}, 6.0 myr^{-1}, respectively (Fig. 7A).

Whereas the protodunes near the start of the transect deform little between 2007 and 2016 across the initial ~ 600 m of the transect, the final protodune examined in the transect deforms significantly between 2007 and 2016 across the last 150 m of the transect (Fig. 7B). At the

time of acquisition of the 2007 dataset, the shape of the last protodune is slightly asymmetrical where the steepest slope faces the NE, and the stoss slope and crest are smooth over tens of meters. In the 2008 dataset, a 40 m long, 10 cm amplitude, symmetric bump is present on the stoss slope that is not present in the 2007 dataset. Comparing the 2008, 2009, and 2010 datasets demonstrates that this bump increases in amplitude and asymmetry with time and becomes the crest of the last protodune by 2010. Over the same period, the previous protodune crest became a bump on the protodune lee slope, and overall, the protodune acquired a strongly asymmetric shape. The 2015 topography data captured at the time of the GPR transect shows the lee-slope bump became the steepest slope visible along the transect. Field observations indicate that the steep lee slope was at the angle-of-repose and was the slipface of the first mature dune. Comparing the 2010 and 2016 datasets also shows a decrease in elevation of the interdune area during the transition to a dune. Overall, comparing the time-series datasets between 2007 and 2016 shows the amplitude and asymmetry of the last protodune increasing, the lee slope of the last protodune steepening to the angle of repose, and the interdune elevation beyond the first mature dune decreasing in elevation.

4.3. Description and interpretation of radar reflections along the 784 m transect

4.3.1. Survey from 0 m to 460 m

Continuous, planar, horizontal to low-angle (< 5°) radar reflections characterize the initial 460 m of the survey transect, and compose radar facies 1 (RF1) (Figs. 8 and 9) (Table 1). Sand patch topography, visible by field inspection, is distinguishable in the RTK data as variable, cm-scale topography above the Alkali Flat surface (Figs. 4C, 7). However,
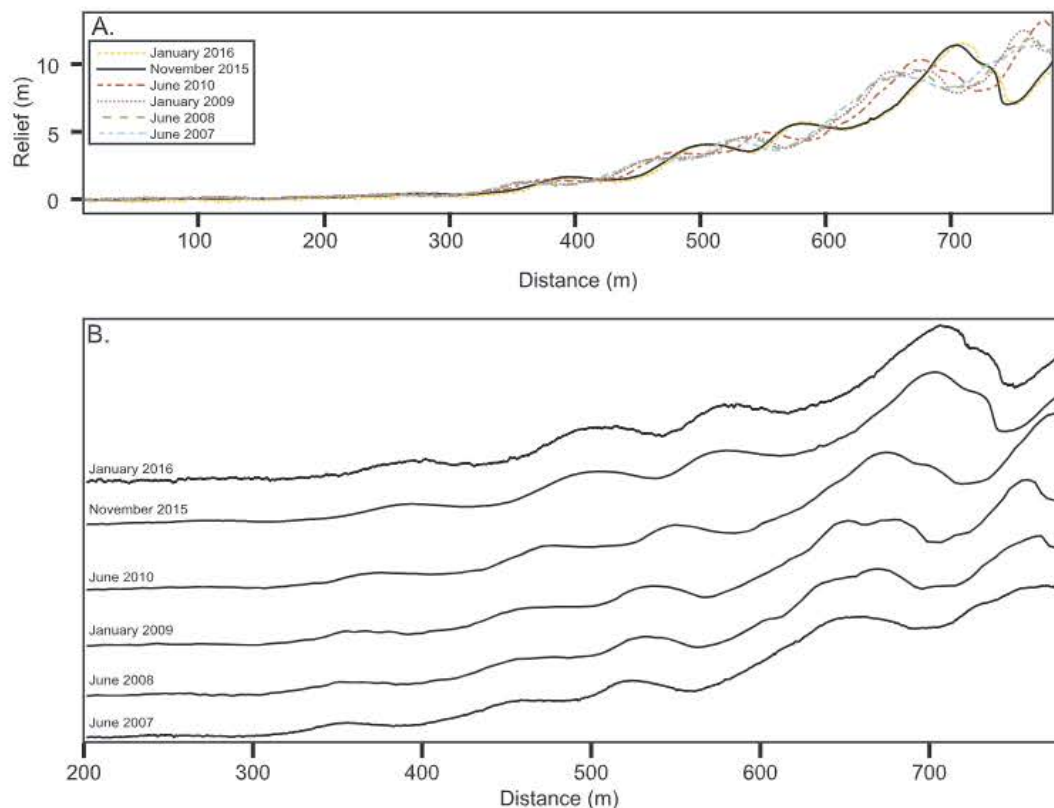

Fig. 7. June 2007-January 2016 topographic profiles of the upwind. (A) All topographic transects overlaid on each other to show temporal shift in topography. (B) All topographic transects plotted by time on the y axis. An overall translation of the topography occurs toward the NE (right on figure). Both spatially and temporally the protodunes increase in amplitude. The most dramatic change in topography occurs with the last protodune around 650 m. On this protodune, the relatively smooth, low-relief, asymmetric profile in 2007 increases in roughness, amplitude, and asymmetry as smaller protodunes form and merge with the larger protodune. Also note the marked change in topography from 2007 to 2016 of the dune at 750 m. Note, the crest of that dune grows in amplitude, but does not shift downwind significantly until after 2010 when the amplitude of the upwind protodune increases.
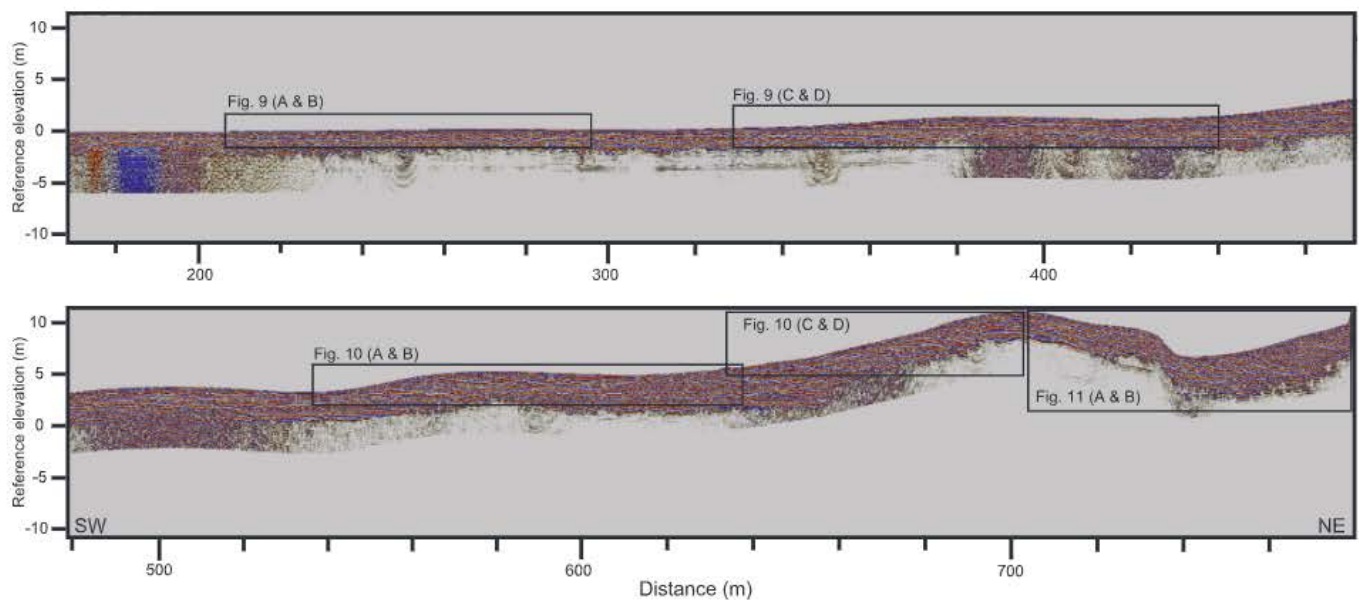
Fig. 8. Topographically corrected GPR data showing all protodunes surveyed along the transect. Location of Figs. 9–11 shown on the figure.

the vertical resolution of the 200 Mhz GPR system prevents internal imaging of the sand patch. Decimeter-scale surface topography marks the appearance of the first protodune between 210 m and 300 m from the start point of the transect. Although not well expressed in the low vertical exaggeration radar image (Figs. 8 and 9A), topography is visible in the vertically exaggerated image of Figs. 4C and 7, and was also apparent in the field. Reflections within the protodune topography are flat lying, matching reflections deeper in the subsurface (Figs. 8 and 9A). The second protodune occurs between 340 m and 430 m. Similar to the first protodune, the internal reflections are flat-lying, but abruptly terminate at the upwind stoss slope of the protodune, and are sub-parallel to shallow-dipping on the leeward side (Figs. 8 and 9C, D). Some of the flat-lying reflections extending from the initial 300 m of the transect terminate at a surface that separates reflections located within the protodune and reflections located below the protodune. The surface appears to be a paraconformity, or a subtle low-angle angular discordance (unconformity type 1 – UC1). Beneath this surface, reflections extend laterally undisturbed. The UC1 surface is flat lying for the first 40 m beneath the protodune, before a subtle drop in elevation, after which the surface appears to gently rise to unity with the modern geomorphic surface. The exact termination of the stratification is masked by noisy data at the NE termination of the protodune.

4.3.2. Survey between 460 m and 630 m

Low-angle reflections (RF1) that reach up to 5° inclination and define the majority this section are juxtaposed with sparse planar, moderately inclined (5°-10°, RF2) and planar, steeply inclined (> 15°, RF3) reflections. The third and fourth protodunes occur within this section and are greater amplitude than the first and second protodunes (Fig. 4C, 18, 10A, B). The third protodune occurs between 460 m and 540 m (Fig. 8). Similar to the second protodune, the stoss slope truncates, and the lee slope parallels, the sub-horizontal internal reflections. A UC1-type surface defines the base of the protodune. Unlike the first 460 m of the transect, where the reflections continue laterally in the subsurface, the RF1 reflections beneath the third protodune are disrupted by subjacent and superjacent UC1 unconformities. This architecture initially appears at the outset of the third protodune (Fig. 8). The steepest low-angle reflections occur within the fourth protodune between 550 m and 630 m with clear NE dipping reflections that downlap onto a surface characterized by a low-to-high angle discordance between reflections internal to the protodune and those below the surface (unconformity surface type 2 – UC2) (Fig. 10A, B).

High-angle reflections (RF3) and unconformities that bound high-angle reflections (UC2) characterize the subsurface below the fourth protodune (Fig. 9A, B). RF3 reflections are truncated by UC2 surfaces at their top terminations and downlap onto underlying UC2 surfaces. The sub-horizontal, low-angle and laterally discontinuous UC2 surfaces bound the RF3 reflections, forming packages of high-angle reflections. Within the packages of RF3 reflections, rare high-angle angular discordances represent unconformity surface type 3 – UC3. These surfaces truncate the upper RF2 reflections and downlap onto bottomsets of the RF2 reflections. UC2 surfaces truncate the UC3 top terminations.

A notable elevation rise of the inter-protodune surface occurs in this section. The inter-protodune surface between protodune 2 and 3 is 1 m above the 0 m reference elevation. This surface rises to 5 m above the reference elevation by the inter-protodune area separating protodunes 4 and 5.

4.3.3. Survey between 630 m and 784 m along transect

An abrupt elevation increase along the stoss slope of the last protodune nearest the first dune characterizes the sand ramp morphology between 630 m and 700 m along the transect (Fig. 10C, D). In the subsurface of the last protodune, NE dipping UC1 type surfaces bound RF1 reflections, which extend parallel to subparallel to the UC1 surfaces. Some SW facing reflections terminate at the protodune stoss slope, whereas others rollover at their SW facing termination, and parallel the protodune stoss slope (Fig. 10c and d). The NE facing terminations either downlap onto the lower UC1 surface, or extend below the depth of radar resolution. This region also marks a rapid elevation increase noted by a 4 m rise over 70 m to reach ~ 11 m above the Alkali Flat hardpan. At 700 m, the topography reaches its zenith at the crest of the last protodune, at which point, the RF1 reflections and UC1 surfaces both have a convex upward shape that mimics the topography (Fig. 10C, D).

Between 700 m and 740 m, the RF1 reflections and UC1 surfaces dip shallowly to the NE before transitioning laterally into RF3 high-angle reflections and UC3 surfaces, respectively (Fig. 11A,B). RF3 reflections visible at the geomorphic surface mark the first appearance of a mature dune slipface at the surface. From 740 m to the end of the transect, RF1 reflections are visible throughout the interdune surface and subsurface and RF3 reflections define the internal geometry of the topographic rise that is the stoss slope of the second dune.
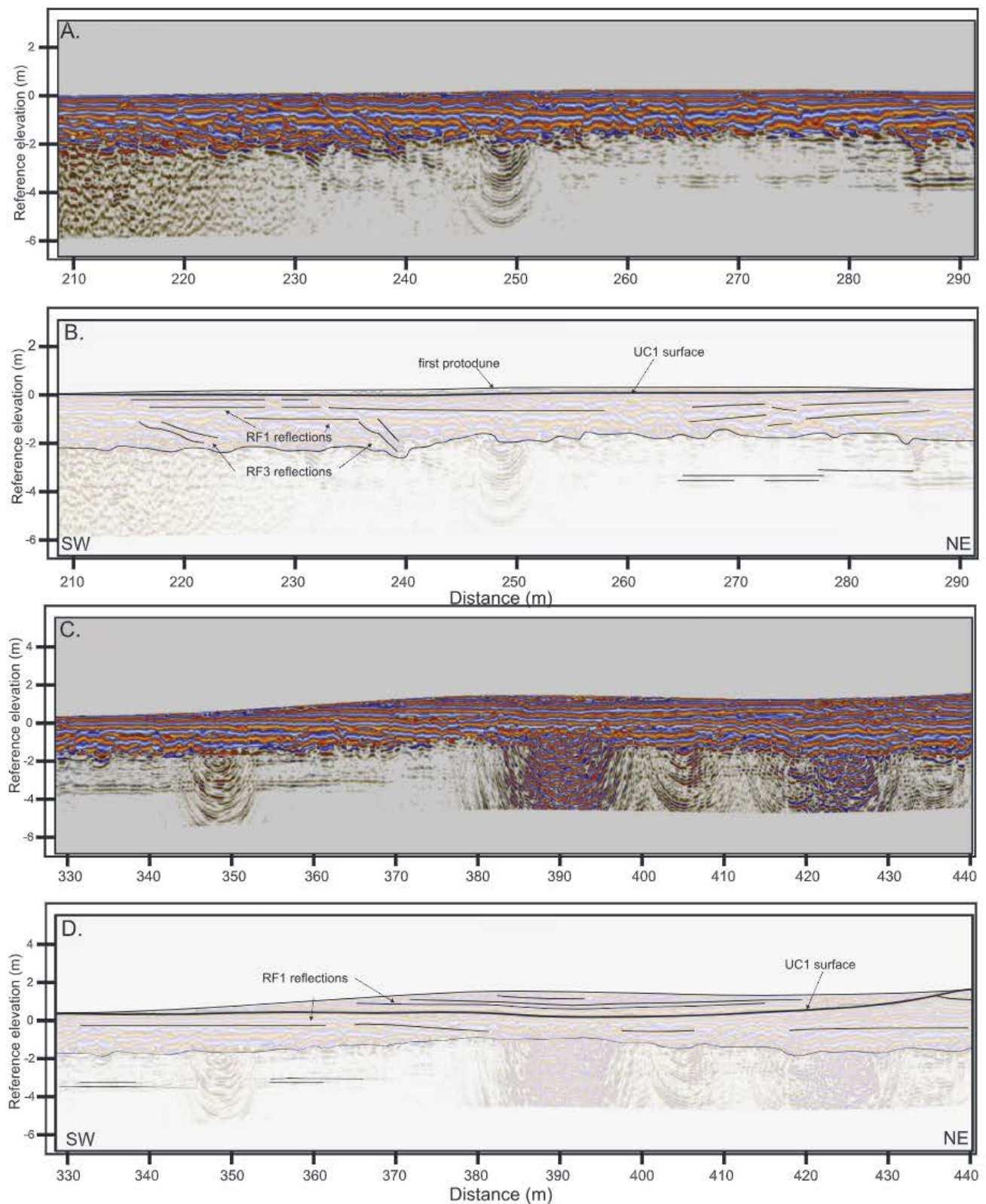
Fig. 9. Detailed view and interpretations of GPR data of the first two protodunes. (A) Uninterpreted and (B) interpreted GPR data of the first protodune. (C) Uninterpreted and (D) interpreted GPR data of the second protodune.

4.3.4. Interpretation of radar reflections and surfaces

The radar reflections and surfaces of the sand ramp transect represent a typical suite of eolian stratification (see Table 1). RF1 reflections are interpreted as Alkali Flat hardpan deposits produced by variable playa processes, as well as, low-angle eolian stratification generated by impact ripple and grainfall processes during sand patch and protodune migration. The presence of impact ripples across the sand patch and protodune surfaces, and pin-stripe lamination in the shallow trench (Fig. 6) supports the latter interpretation. Field observations of impact ripples and grainfall in the lee of the highest

Table 1
GPR radar facies.

Type	Description	Interpretation
RF1	continuous, planar, horizontal to low-angle reflections (< 5°)	stratification formed from playa processes, wind ripple stratification from sand patches, wind ripple and grainfall stratification from protodune migration
RF2	discontinuous, planar, moderately inclined reflections (5-10°)	protodune stratification, oblique view of RF3 stratification, toesets of RF3 stratification
RF3	discontinuous, steeply inclined reflections (> 15°)	dune cross-stratification composed of wind ripple, grainfall, or grainflow stratification
UC1	Horizontal-to-low inclined reflection, parallel to low angular discordance between reflections	paracomformity arising from sand patch and protodune movement bypass surface, reactivation surface, protodune interaction surface
UC2	Horizontal-to-low inclined reflection, moderate to high angular discordance between reflections; bound RF3 reflections	first-order set bounding surfaces
UC3	Moderately-to-steeply inclined reflections, low to moderate angular discordance between high angle reflections	Dune reactivation surfaces

amplitude protodunes support a wind ripple and grainfall stratification interpretation for high-angle RF1 reflections.

RF3 surfaces are interpreted as dune cross-stratification. The presence of high-angle reflections associated with the mature dune slipface (Fig. 11) support this interpretation. This subsurface interpretation is consistent for the Alkali Flat region, where dune cross-stratification characterizes the surface westward of the first dune, indicating the presence of a prior active dune field (Szynkiewicz et al., 2010; Kocurek and Ewing, 2016). The origin of RF2 is not clear, but could represent either the steep lee slope of a protodune, an oblique view of a steeply dipping RF3 reflections, or perhaps the basal tangential portion of RF3 reflections, where the overlying stratification is truncated.

UC1 surfaces are interpreted as bypass surfaces or, perhaps, subtle erosional surfaces generated by the passage of a sandpatch or protodune (Figs. 8–10). However, erosion in the lee of a protodune is likely minimal to nonexistent because flow remains largely attached across the surface (flow expansion and minor flow separation occurs for the highest amplitude protodunes; Kocurek et al., 1992). UC2 surfaces are interpreted as first-order bounding surfaces (cf., Brookfield, 1977; Kocurek, 1981) generated by the migration of mature dunes. This interpretation is consistent with the sub-horizontal, laterally discontinuous geometry of these surfaces and their association with RF3 reflections. UC3 surfaces are interpreted as reactivation surfaces formed within a set of dune cross stratification. Some UC1 surfaces could be protodune reactivation surfaces. For example, in the lee of the last protodune, UC1 surfaces transition laterally to the NE into UC3 surfaces (Fig. 11). Given the high frequency of dune-dune interactions, such as mergers and lateral linking resulting from dune collisions, at the upwind margin (Ewing and Kocurek, 2010), some of these surfaces may represent protodune and dune interaction surfaces that result from collisions between dunes (e.g., Brothers et al., 2017).

5. Discussion

5.1. Relating GPR reflection geometries and sand ramp topography

The geometry of reflections across the transect, from SW to NE, show flat-lying strata transitioning to angle-of-repose strata. Fig. 12 presents the spatial change in the apparent dip angles along the transect, color-coded from the digitized GPR reflections (Fig. 12A, B), and a scatter plot of apparent dip angles over transect distance (Fig. 12C). Reflections within the surface bedforms remain less than 5° (RF1) until the last ~ 100 m of the transect, where they transition to moderately dipping (RF2) and then to steeply dipping (RF3). The change in reflection geometry at the surface (i.e., solid circles, Fig. 12C) corresponds to a spatial change in the surface morphology, whereby sand patches transition to protodunes, which give way to mature dunes. An increase in protodune amplitude along the transect, corresponds with an increase in the RF1 dip angles. This is particularly notable in protodune 2, centered around 550 m, and the last protodune, protodune 1, between 650 m and 700 m. High-angle reflections at the end of the

transect correspond to the slipface of the first dune. Still, there remains only minor moderate-angle reflections before the onset of an angle-of-repose lee face.

Subsurface radar reflections show a wider range of dip angles than those of the active surface bedforms. RF1 reflections within the first half of the transect are low-angle, similar to the surface morphology, however, reflections around 500 m dip at angles ranging from a few degrees to 23°. The steeply dipping reflections in the subsurface end around 650 m where they are lost beneath the last protodune because the GPR did not penetrate to the depth required to image the strata.

To examine protodune dynamics and the origin of the GPR reflections along the transect, time-series topographic profiles were overlaid onto the GPR transect (Fig. 13). The spatial correlation between the prior protodune lee slopes and the low-angle strata that characterize the protodune deposits supports the hypothesis that migrating protodunes generate low-angle strata. Along the transect, the steepness of the protodune strata increases, along with the protodune amplitude. The steepness of the strata increases across the first four protodunes despite the shape of these protodunes remaining symmetric to slightly asymmetric. The protodune troughs match, in some areas along the transect, the location of UC1 surfaces indicating that the protodune troughs generate low-angle bounding surfaces as the protodunes migrate (Fig. 13). Crest and trough trajectories measured between 2007 and 2015 range from 0.5° to 1.2° along the first 650 m of the transect (n = 10), and up to 2.5° between 650 m and 700 m along the transect (n = 4) (Figs. 7, 13B, C). Stoss slope angles measured on the 2015 profile are 1°, 2°, and 2.5° for protodunes 4, 3, and 2 respectively, and 3.5° at protodune 1. The steep upward trajectory of the last protodune crest visible between successive time periods indicates that the angle of bedform climb (e.g., Rubin and Hunter, 1982) of the last protodune is higher than the initial protodunes (Fig. 13C). The stratal geometries of the last protodune that show topset rollover support this interpretation (Figs. 10 and 13). Moreover, the angle of climb is 70% of the stoss slope angle, which is a near critical angle of climb (i.e., near the stoss slope angle, Rubin, 1987).

5.2. Protodune development and the accumulation of protodune strata

The stages of protodune development depicted here are broadly consistent with those described in Kocurek et al. (1992) and Elbelrhiti (2012), and more recent studies by Baddock et al. (2018). For example, sand patches transition to low-relief slipfaceless protodunes that become steeper and show asymmetric form before developing a slipface, which indicates a mature dune (Fig. 14A-C). Exceptions from prior models exist, however. The protodunes emerge from poorly sorted sediment within a largely transport-limited environment (minor exposure of availability-limited interdune protodune substrate) whereas the protodunes described by Kocurek et al. (1992) Elbelrhiti (2012), and Baddock et al. (2018) emerge from well-sorted sediment within a strongly availability-limited (e.g. Kocurek and Lancaster, 1999) environment.
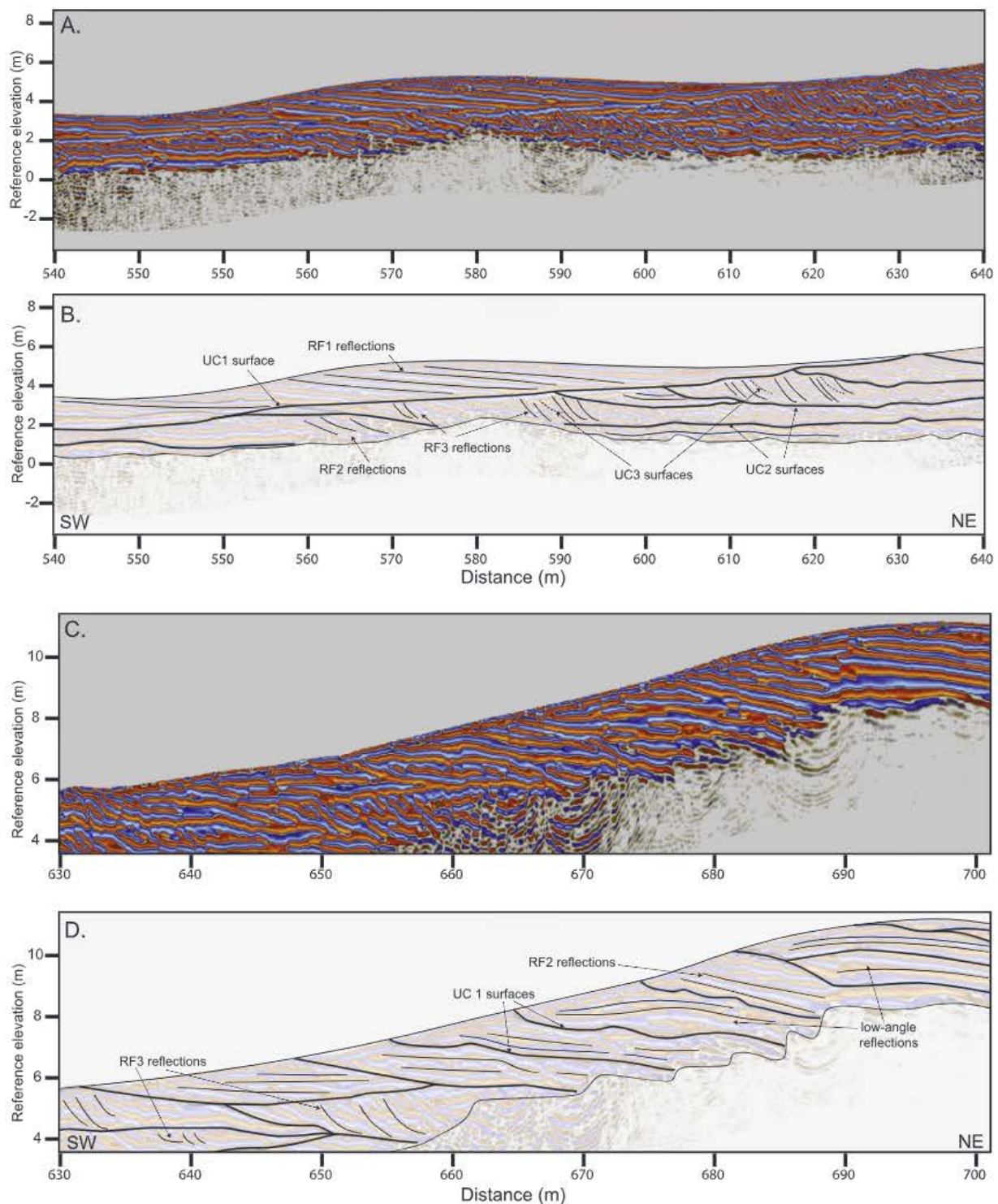
Fig. 10. Detailed view and interpretations of GPR data of the fourth and fifth protodunes. (A) Uninterpreted and (B) interpreted GPR data of the fourth protodune. (C) Uninterpreted and (D) interpreted GPR data of the fifth protodune.

Strong selective transport at the upwind margin manifests as discrete coarse-grained and impact ripple patches near the start of protodune emergence that are at the approximate wavelength of the protodunes (Fig. 14A). The role of the ripple patches in the initiation of the protodunes is not clear, but the development of protodune topography noticeably influences the spatial distribution of the sand patches. Coarse-grained ripples preferentially form on the protodune stoss slopes upwind of the protodune crest, and impact ripples and grainfall preferentially form on the lee slopes (Fig. 14B). Concentrations of the >

1 mm sand fractions upwind of the crest arise because gravity prevents the transport of the coarsest grains from moving up the stoss slope and across the protodune crest (cf., Fenton et al., 2017). The coarse-grained patches could also signal the locus of the maximum shear stress upwind of the crest, which is thought to be a requirement for the growth of the of protodunes into mature dunes (Andreotti et al., 2002; Claudin et al., 2013). Accelerating flow up the protodune stoss slope also winnows the medium grains leaving a lag of coarser grains. Flow expanding downwind of the protodune crest deposits the winnowed medium sand
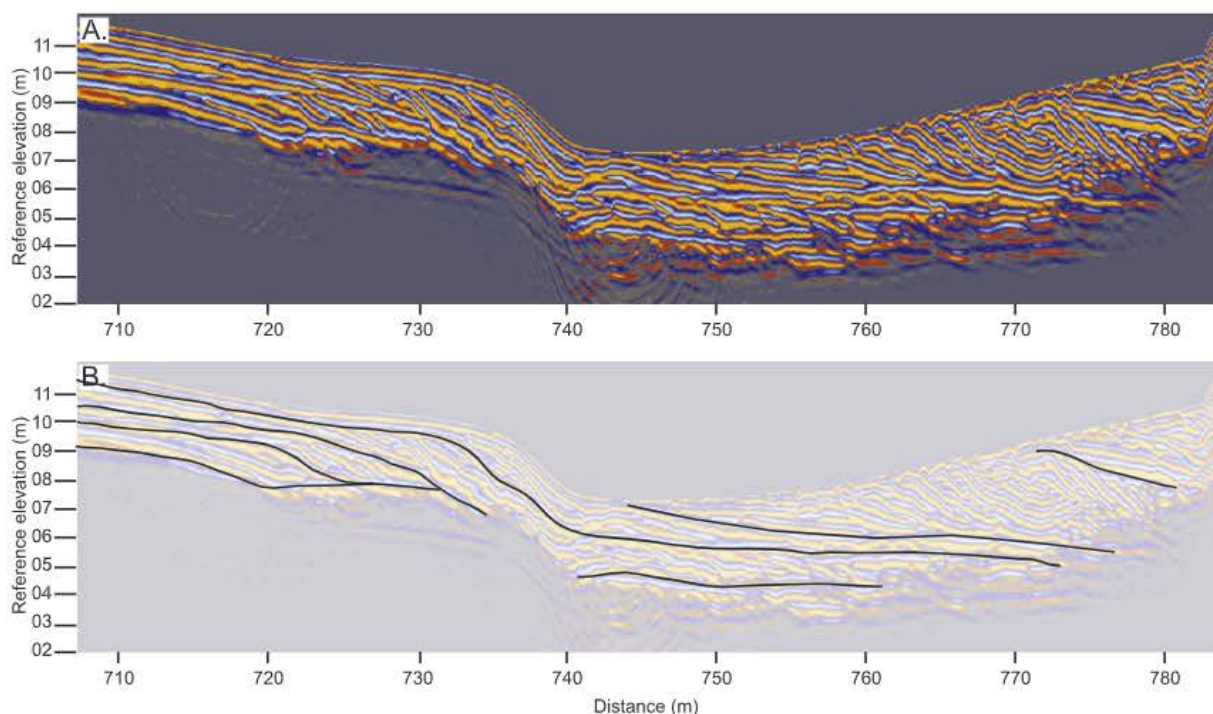
Fig. 11. Detailed view and interpretation of GPR data of slipface formation. (A) Uninterpreted and (B) Interpreted GPR data of slipface formation.
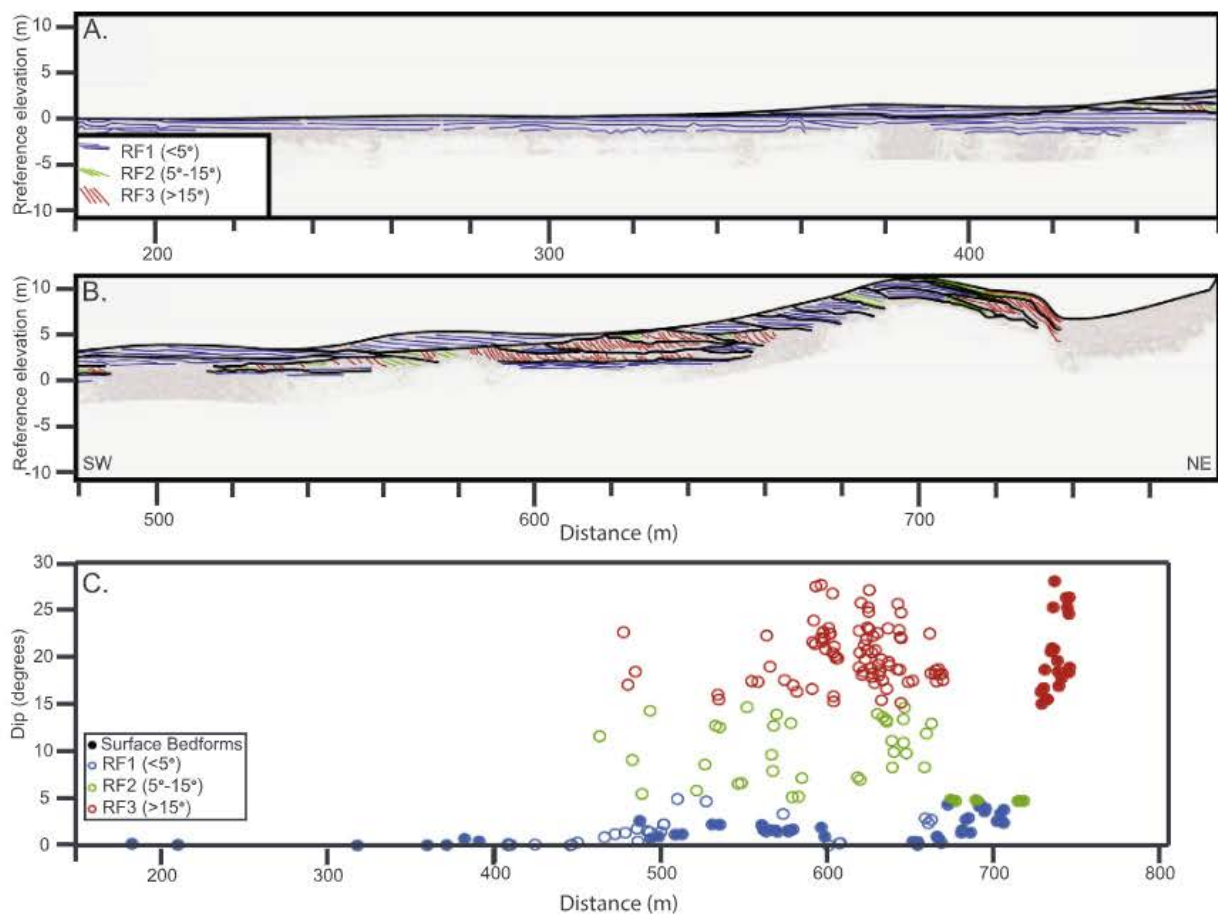

Fig. 12. Digitized and measured GPR reflections across the transect showing different radar facies. (A) and (B) Digitized RF1 (blue, < 5°), RF2 (green, 5°–10°), and RF3 (< 15°) reflections showing changes in the reflection dip across the transect. (C) A scatter plot showing the change in dip of the reflections within the surface bedform (solid circles) and in the subsurface (open circles) for each radar facies.
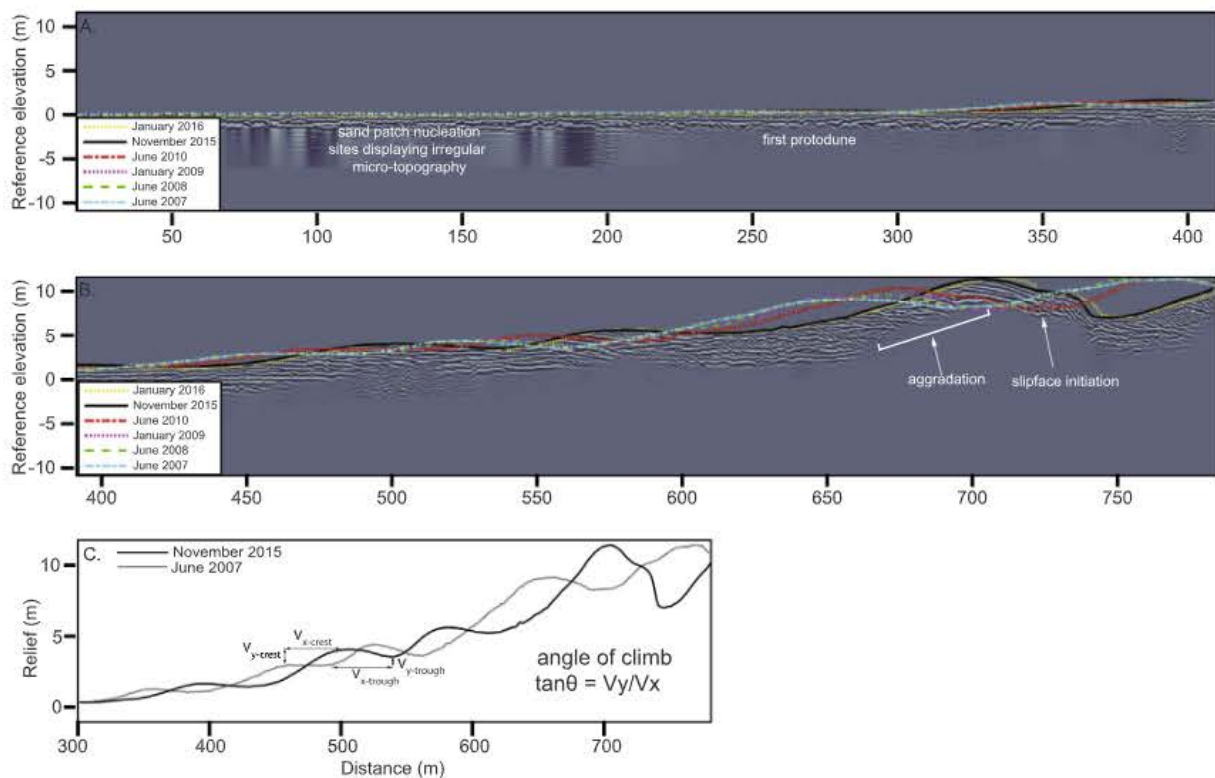
Fig. 13. Time-series topography overlain on GPR data across the upwind margin transect. (A) Microtopograhy related to sand patch nucleation is not distinctive, whereas topography of the first and second protodunes distinctively translate downwind. The topography of the second protodune correlates to the GPR reflections visible within the second protodune. (B) Protodune and dune topography correlate well to GPR reflections. Notably, reflections interpreted as protodune foresets match well with topographic profiles acquired prior to the GPR data. (C) Upwind margin profiles from 2007 (gray) and 2015 (black) showing how angles of climb were measured in the protodunes per Rubin and Hunter (1982).

creating impact ripples and grainfall. Depositing the medium sand fraction in the lee of the migrating protodunes generates strata composed of medium sand. The discrepancy between the surface coarse and subsurface medium sand generates a stratigraphic architecture similar to zibars described by Nielson and Kocurek (1986)

The 88 m average stoss-to-lee wavelength (n = 5, measured as length) of the protodunes measured at White Sands is greater than the wavelengths reported in other protodune studies. For example, Kocurek et al. (1992) reported an average wavelength of ~28 m (average value derived from ~26 values measured from Fig. 12a of Kocurek et al., 1992). Elbelrhiti et al. (2005) reported average wavelengths of 20 m and 28 m (for two populations of protodunes). Elbelrhiti (2012) reported an average wavelength of 17 m.

Could the wide range of grain sizes account for the difference between protodune wavelength at White Sands? The protodunes in the above referenced studies form from ~0.18 mm sand, whereas the protodunes at White Sands form from d_{50} 0.67 mm and 0.23 mm sand populations that compose the sand ramp. Based on the drag length scaling relationship with saturation length (Hersen et al., 2002; Claudin and Andreotti, 2006; Andreotti et al., 2010), the protodune wavelength predicted to form from the coarse sand is ~78 m, and the protodune wavelength predicted to form from the medium sand is ~26 m. The coarse sand that covers the surface of the sand ramp, thus, dictates the dominant wavelength of the protodunes despite the medium sand found on the interior of the protodunes. Although the ~88 m protodune wavelength characterizes the dominant protodune wavelength on the sand ramp, the protodunes are not all of the same size. Sparsely and irregularly distributed, shorter wavelength protodunes are present on the sand ramp (Figs. 1E, 7B). Their ~20 m wavelength matches that predicted for medium sand and the protodunes present on the stoss slopes of dunes within the dune field (Fig. 1C). Overall, two distinct wavelengths of protodunes arise from the fractionation of sand into

coarse and medium populations along the sand ramp.

The protodunes increase in wavelength (76 m to 122 m), amplitude (0.2 m to 4.0 m), and migration rate downwind (3.2 m/yr to 6.1 m/yr). Notably, wavelength varies only by 60%, whereas amplitude varies by a factor of 20 and migration rate varies by a factor of 2. The wavelength-amplitude relationship has not been previously reported, but matches, somewhat, with the expected co-evolution of these bedform parameters (e.g., Ashley, 1990), although Baitis et al. (2014) showed that this relationship is poorly developed within the White Sands Dune Field. The wavelength-amplitude trend is forced principally by the growth of last protodune, which increases significantly in height and wavelength compared with the upwind protodunes. Aggradation, protodune merging, and growth of a slipface likely account for this outlier. In the absence of the last protodune, the wavelength of the upwind protodunes remains similar at an average 80 m, which is close to the predicted wavelength of 78 m based on the drag length scaling relationship. Excluding protodune 1 also changes the wavelength-amplitude relationship whereby wavelength remains stable and protodune amplitude increases; a relationship not reported in other bedforms. The trend in migration rate shows a linear increase over the transect as compared to wavelength and amplitude, but nonetheless increases commensurate with the increase in wavelength and amplitude. From a process perspective, the increase in migration rate is consistent with the observation of increasing amplitude and steepness that could make sand trapping more efficient. The minimal variability of these parameters prior to the transition to slipface development may signal the robustness of the saturation length instability tied to the development of protodunes. The fluid-grain feedbacks that generate such an instability could remain the dominant control on protodune morphology until the protodunes reach a threshold amplitude and steepness after which wind flow expansion or separation in the protodune lee dominate changes in the protodune. After flow separation, feedbacks between the
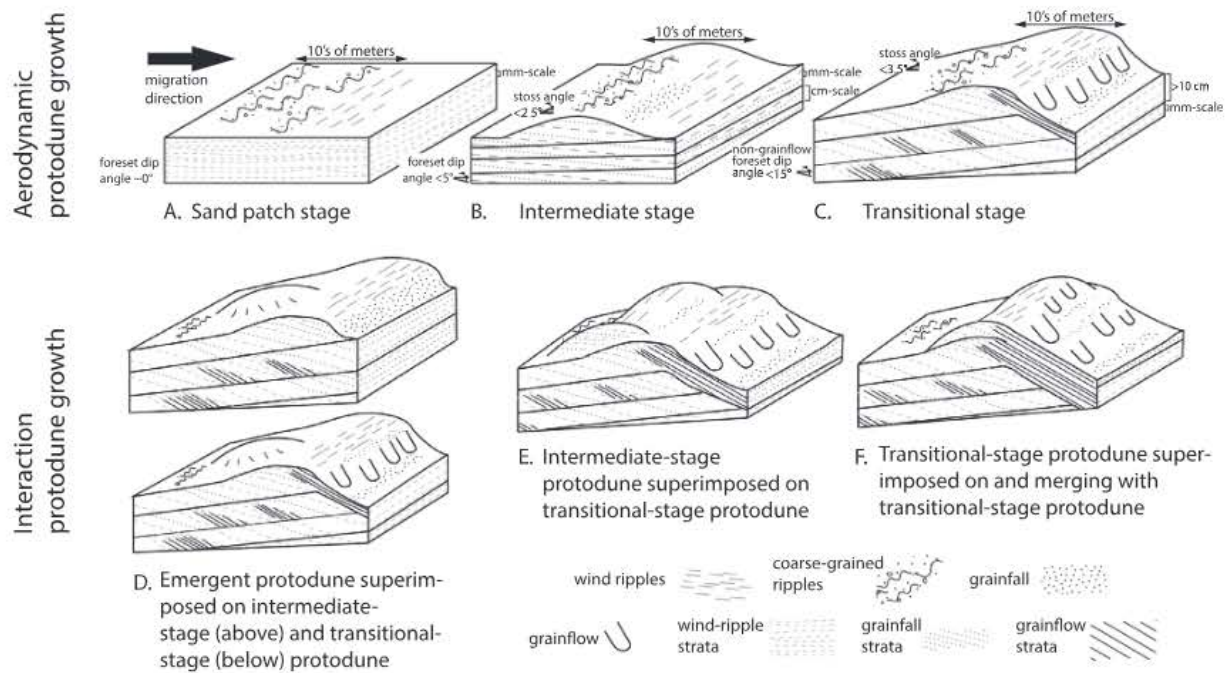
Fig. 14. Schematic showing stages of protodune growth and expected cross-stratification. (A-C) Model of protodune growth by aerodynamic-topographic feedbacks. (A) Patches of impact- and coarse-grained ripples organize at length-scales of 10 s of meters and form deposits of planar, parallel stratification. (B) Intermediate-stage protodune with coarse-grain ripples formed on the stoss slope near the crest. Wind ripples and sparse grainfall form in the lee. Strata within the associated deposit form at angles less than 5°. This stage is comparable to Kocurek et al. (1992) stage C. (C) Transitional phase of a protodune to a mature dune. Coarse-grained ripples persist on the upper stoss slope, but give way to wind ripples near the dune brink and ultimately grainfall and grainflow in the lee as the slipface develops. The stratigraphic architecture of the deposit includes low-angle strata with rare high angle strata that represent temporary initiation of a slipface. (D-F) Model of dune growth from dune interactions whereby a protodune superimposed on another protodune develops a slipface that merges with the slipface of the host protodune. (D) Two possible initial conditions for the growth of a superimposed protodune on an intermediate-stage protodune or transitional-stage protodune. (E-F) Growth in the height of the superimposed protodune manifests into an overall increase in height of the compound form, which, through merging of the transitional-stage protodunes, increases the size of the slipface and scour into the underlying deposits.

flow and evolving form that give rise to dune deformation and dune interactions could disrupt the consistent relationship between wavelength and amplitude and drive the system rapidly toward mature dune development. This is consistent with the abrupt change from protodunes to dunes over the last 100 m of the transect.

The relationship between the measured stratal geometries and the evolving protodune topography from 2007 to 2016 indicate that protodune migration generates low-angle stratification (Figs. 13 and 14). Flat-lying and nearly flat-lying wind ripple stratification developed as the nascent protodunes migrated. The growth in protodune amplitude and asymmetry coincides with increased steepness of the lee face, as indicated by the measured stratification angles (Fig. 12). Thus, the increased steepness of the protodune strata implies maturation of protodunes over time and space, which contributes to the development of mature dunes.

As with the mature dunes in White Sands, the protodunes of the upwind margin are subject to variable seasonal wind regimes, however, the impact of the variable wind regime on protodune morphology and stratification is not clear (Ewing et al., 2015; Pedersen et al., 2015; Swanson et al., 2016, Gao et al., 2018). The variable wind regime at White Sands creates along-crest migration of dune sinuosity and erosional surfaces on dunes (Ewing et al., 2015; Pedersen et al., 2015; Swanson et al., 2016). These changes in dune shape manifest as reactivation surfaces in the dune strata (Kocurek et al., 2007). Protodune shape likely responds similarly to the variable wind regime forming reactivation surfaces. The best candidates for protodune reactivation surfaces are the bounding surfaces that define the most aggradational part of the transect around 650 m (Fig. 10C, D, 11A, and B). These surfaces parallel the dip direction of the strata and could reflect erosion of the protodune lee slope by northerly winds (cf., Pedersen et al., 2015). Alternatively, or in addition to, these may represent protodune

interaction surfaces whereby protodunes merge, as is supported by the presence of compound protodunes in the topographic profiles (Fig. 7).

The principles of bedform climb (Rubin and Hunter, 1982) apply to protodunes and account for the development of low-angle stratification along the transect. The absence of a clear link between the sand patch and protodune topography and the underlying strata indicate the initial sand patches and protodunes mostly bypass across the underlying sand ramp surface. Although some climb of the protodunes is documented (Fig. 13C), any substantial accumulation of low-angle stratification in this region of the sand ramp likely reflects fill of antecedent scours on the underlying sand ramp surface rather than from a significant rise in the accumulation surface. The first distinct accumulation of sediment related to a protodune occurs within the third protodune, as evidenced by a paraconformity between low-angle dipping stratification. Based on the correlation between the time-series topographic profiles and the GPR data that shows the migration of the inter-protodune troughs (Fig. 13), these surfaces could represent interdune surfaces (e.g., Kocurek, 1991; first-order bounding surfaces of Brookfield, 1977), however reactivation surfaces (e.g., Kocurek, 1991; 3rd order bounding surfaces of Brookfield, 1977), or bypass surfaces cannot be ruled out.

The accumulation of sediment in the final few hundred meters of the transect that corresponds to the development of the protodunes into mature dunes likely arises due to several factors. Field observations indicate that, as the protodunes increased in amplitude, they trap more of the medium sediment fraction on the lee face, which is consistent with the expected increase in flow expansion and deceleration (e.g., Kocurek et al., 1992). An increase in amplitude could increase the feedback between airflow and protodune shape resulting increased sediment trapping efficiency and aggradation of the bedform (Fig. 14A-C). In this scenario, a decrease in the spatially averaged bulk volume sediment transport rate occurs as the efficiency of sediment trapping by

the protodunes increases (i.e., less sediment bypasses). The result, per Allen (1970) and Rubin and Hunter (1982), is the net deposition rate in the vertical direction (Vz) increases relative to the rate of bedform migration across the accumulation surface (Vx).

Protodune collision and merging likely enhance the growth protodunes (Fig. 14D-F). The similar migration rates of the large protodune precludes significant merging among that size population, but smaller, transient protodunes formed from the medium grain size would migrate relatively faster and could merge with the larger protodunes. Similarly, protodune-dune and dune-dune interactions could play a role in aggrading sediment (Fig. 14D-F). This would be most effective at the transitional zone where the first slipfaces develop. Lastly, the vertical transition from flat-lying topography to over 10 m dunes over the transect length has been previously considered to generate landscape roughness and the development of an internal boundary or mixing layer that drives flow deceleration near this transition (Jerolmack et al., 2012; Anderson and Chamecki, 2014). This large scale aerodynamic effect could lend to spatial decrease in flux across the ramp, the initial deposition of sand on the ramp, and the aggradation of protodunes over a short spatial distance.

Overall, the GPR data reveal that dune cross-stratification composes most of the sand ramp, and the ramp is not primarily a consequence of accumulation of low-angle stratification from protodune migration. Rather, most of the sand ramp topography appears to be an erosional surface due to the NE migration of the dune field, whereby the protodunes leave little accumulation on the surface. Because the GPR did not penetrate sufficiently deep to resolve stratigraphy beneath the final protodune, the relative contribution of protodune aggradation and an increase in the slope of the underlying topography to the 4 m rise in topography remains unclear. However, the evolution of the topography highlights that, regardless of a possible increase in the slope of the underlying topography, aggradation of the protodune stratigraphy plays an important role in transition to mature dunes.

5.3. Slipface formation

The simplest model for slipface formation, in which a progressive increase in protodune amplitude and lee slope steepness drives flow separation and sediment trapping (e.g., Kocurek et al., 1992), conveys only a part of the dynamics at White Sands. Morphology, stratigraphy, and grain size distribution all point to a complexity of processes involved, including selective transport, protodune deformation, and protodune and dune interactions.

Topographic profiles from the last 100 m of the transect show that the increase in amplitude and asymmetry at the last protodune occurs, in part, by merging protodunes (Figs. 7, 13, 14D). The largest protodunes migrate at a constant rate, while smaller protodunes migrate relatively faster overtaking the larger protodunes and becoming trapped on the lee face. In such a way, one large protodune can host smaller protodunes (Fig. 14D). Fig. 7 shows the presence of two bumps, which are smaller protodunes, on the larger, last protodune. The merger of these smaller protodunes with the larger protodune facilitated the development of two slipfaces (visible in January 2016 profile shown in Fig. 7B). Merger of the two slipfaces into a single, larger slipface would generate a dune of comparable size with the 4–5-m high dunes positioned downwind of protodune one (Fig. 14E,F). Notably, the time-series topography data from 2007 to 2016 also show that, as the slipface developed, leeside scour into the interdune increased, thus increasing the relative slipface height, and contributing to the negative climb of the first dune (Fig. 7 and 14D-F). Thus, protodune merging characterized by different median grain sizes produced an increase in amplitude, asymmetry, and grain trapping, all of which led to slipface formation.

The GPR data of the strata that represent slipface formation indicate that multiple slipfaces appeared and disappeared as part of the slipface building process (Fig. 11). A package of high-angle strata visible at the

base of protodune 1 indicates initial slipface development. This package indicates ~10 m of slipface migration. A low-angle bounding surface interpreted as a reactivation surface truncates the package and indicates beveling and removal of the slipface. High-angle strata that superpose this surface indicate a second slipface forming and migrating over the beveled surface. A second erosional surface superposed by high-angle strata indicates beveling of the second slipface and forming of the modern (2015) slipface. Beveling and erosion of the slipfaces could occur by seasonal changes in wind conditions (i.e., reactivation surfaces) or dune interactions, which are abundant in the first 500 m of the dune field (Ewing and Kocurek, 2010). Lateral linking and merging are the dominant constructive dune interaction in this area of the dune field and splitting is the dominant destructive interaction (Ewing and Kocurek, 2010). Such interactions between protodunes and/or nascent dunes could promote or deter slipface formation by adding volume to a small protodune, splitting a protodune nearing slipface formation, or deforming the shape of a protodune. Overall, the role of interactions at the protodune-dune interface is not yet understood. The comings and goings of the slipface show that development does not guarantee maturation of a protodune into a dune. The slipface must become sufficiently large to withstand variations in the wind regime or collisions with other protodunes or dunes.

The combination of merging protodunes that form multiple slipfaces that themselves merge and generate significant lee side scour represents a new model for rapid dune growth during the first stages of the dune field development (Fig. 14). The model shown here is more complex than the typical model of dune growth in which dune height progressively increases with grain trapping driven by decelerating flow upwind of the crest that leads to slipface formation. Protodune merging provides a mechanism to abruptly increase protodune amplitude thereby generating flow expansion and separation and scour, which in turn, provides a robust sand trapping mechanism that could lead to slipface development. Slipface merging signals the onset of the non-linear coarsening mechanism that dominates the long-term growth of a dune field. Initial slipface merging plays a clear role in dune growth in the line-source example shown here, likely tantamount to the role it would play in dune formation from a plane source. In a plane source, spatial variability in slipface growth would emplace efficient sand traps throughout the sandsheet and drive an abrupt field-scale shift from a landscape dominated by protodunes to one dominated by small dunes. Thus, just as the transition from protodune to dune is shown here to be spatially abrupt, it is likely temporally abrupt in a plane source. Lastly, the lee scour that occurred during the protodune-to-dune transition demonstrates that cannibalization of the substrate contributed significantly to dune growth. In the example shown, lee scour of ~ 1 m occurred as the dune crest grew by ~ 2.5 m indicating that scour contributed to 40% of the overall increase in dune height. Thus, where sediment is available, substrate cannibalization likely plays a large role dune growth; one that could be comparable to coarsening mechanisms, such as merging. In contrast, cannibalization would be tempered in availability-limited environments thereby allowing the coarsening mechanism to dominate growth.

5.4. The extent of applicability of White Sands to other locations and relationship of protodune stratification to sand sheet deposits and the rock record

The upwind margin of White Sands Dune Field is a unique setting, but the protodune and dune formation processes that occur there apply similarly to other upwind margins, and to the onset of dune field formation. Dune fields originating as a point or line source (e.g., Ewing and Kocurek, 2010) must possess protodunes at their upwind margins (e.g., Fig. 1). Protodunes must also emerge in plane-sourced dune fields, as described by Cooper (1958), Kocurek et al., (1992), and Ping et al., (2014). Given that many dune fields arise from fluvial sediment sources, which are typically coarser and more poorly sorted than eolian

deposits, the selective transport processes that play a significant role in generating protodunes and creating slipfaces at White Sands are likely important in the formation of other dune fields. How transport- vs. availability-limited environments affect protodune growth, migration, deformation, and slipface development remain poorly understood. Similarly, the role of complex wind regimes on protodune development remain poorly documented and understood (Gadal et al., 2017). Continued field-scale experiments (e.g., Ping et al., 2014) and further field observations are needed to understand the roles of selective transport, sediment availability, and wind regime on protodune formation and dune field initiation.

Stratigraphic architectures measured within the protodunes at White Sands closely match some of those attributed to sandsheet strata (Fryberger et al., 1979; Kocurek and Nielson, 1986; Loope, 1984; Porter, 1986; Chan, 1989). As protodunes migrate, low- to moderate-angle strata form, which include wind ripple stratification and low-angle bounding surfaces. In sand sheets, similarly described strata arise from deposition in the lee of small topographic features such as antecedent topography, wind-scoured hollows or blowouts, and vegetation. The strong spatial grain sorting and presence of coarse-grained and impact ripples associated with protodune emergence at White Sands also matches sandsheet descriptions of discontinuous coarse-grain lag deposits, such as the 'poured-in texture' of Fryberger et al. (1992) and zibar stratification of Nielson and Kocurek (1986). Protodune migration thus appears to be an underappreciated part of a greater suite of processes that lend to sand sheet stratification.

Low-angle strata (i.e., sand sheet strata), are recognized to form at the base of some ancient eolian sequences (Loope, 1984; Kocurek and Nielson, 1986, Porter, 1986; Mountney, 2006). Such strata could originate from protodune migration, but such an interpretation would require supporting context and facies associations. For example, saline, evaporitic, sabkha-like conditions (e.g., Jurassic Entrada Formation) that would limit vegetation growth, along with an absence of bioturbation, would lend to the interpretation that the low-angle strata formed from protodune migration. Laterally discontinuous high-angle stratification adjacent to low-angle stratification and suprajacent high-angle stratification would also contribute to such an interpretation by signaling a spatial and temporal transition to mature dunes.

Recognizing protodune stratification in the ancient record could provide a strong morphodynamic context for developing sand sheets. For example, grain size, by its relation to the protodune size, will affect lateral continuity of low-angle stratification and the thickness of the sets. The steepness of the low-angle strata indicates the proximity in space or time to dune development. All the conditions of preserving eolian accumulation must apply to protodunes and, given the documentation of the substantial scour occurring with the onset of slipface formation in this study, it is unlikely that extensive protodune strata are preserved.

6. Conclusion

Protodunes emerge at the upwind margin of White Sands Dune Field from a flat sand bed and, over the course of several hundred meters, transition into fully developed dunes. Decameter-scale protodunes grow downwind in wavelength, amplitude, and migration rate. A mature dune slipface emerges from the highest amplitude and last protodune. Selective grain transport and sorting at the upwind margin into coarse ($d_{50} = 0.67$ mm) and medium ($d_{50} = 0.23$ mm) sand appears to play a role in the formation of the protodunes and the slipface. The coarse grains cover part of the surface as coarse-grain ripples and determine the dominant protodune wavelength, and the medium grains concentrate in the protodune lee slope and the slipface, and compose the protodune deposits.

The correlative relationship between time-series topographic profiles and protodune strata show that migrating protodunes generate low-angle strata. Protodune strata increase in steepness as the

protodunes grow in amplitude, and thus the steepness of low-angle eolian bedding implies the proximity to dune stratification. Minor accumulation of low-angle stratification occurs prior to an abrupt increase in protodune amplitude, which is marked by near critical angles of bedform climb. The abrupt aggradation appears to arise by aerodynamic sand trapping and protodune merging. Protodune interactions are facilitated by the selective transport that generates two grainsize populations and two protodune populations. The medium-grain fraction creates smaller, transient protodunes that merge with the larger stable protodunes. Protodunes mergers appear to play a role in slipface development by increasing the amplitude and lee side sand trapping ability of protodunes. This represents a new model for protodune formation to explore in future work.

Protodune stratification has many hallmarks of sand sheet stratification and appears to be part of a greater suite of processes that generate sand sheet stratification. Unlike the panoply of processes that might promote sand sheet development by the hindrance of dune growth, protodunes have distinct morphodynamic feedbacks between sediment, transporting fluid, and the evolving form which dominate the growth and development of protodunes. This is most apparent by the protodune and dune deformation and interactions that occur at the protodune-to-dune transition. Although protodune stratification has not been identified in the eolian rock record, per se, low-angle stratification found at the bases of eolian sequences could be reasonably interpreted as protodune strata, thus marking the initiation of a dune field.

References

Allen, J.R.L., 1970. A quantitative model of climbing ripples and their cross-laminated deposits. Sedimentology 14 (1–2), 5–26.

Allen, B.D., Love, D.W., Myers, R.G., 2009. Evidence for late Pleistocene hydrologic and climatic change from Lake Otero, Tularosa Basin, south-central New Mexico. New Mex. Geol. 31 (1), 9–25.

Anderson, W., Chamecki, M., 2014. Numerical study of turbulent flow over complex aeolian dune fields: the White Sands National Monument. Phys. Rev. E 89 (1), 013005.

Andreotti, B., Claudin, P., Douady, S., 2002. Selection of dune shapes and velocities Part 1: dynamics of sand, wind and barchans. Eur. Phys. J. B-Condensed Matter Complex Syst. 28 (3), 321–339.

Andreotti, B., Claudin, P., Pouliquen, O., 2010. Measurements of the aeolian sand transport saturation length. Geomorphology 123 (3), 343–348.

Annan, A.P., 2003. Ground Penetrating Radar Principles. Procedure & Applications Sensors and Software, Mississaugua, ON, Canada.

Annan, A.P., 2009. In: Ground Penetrating Radar Theory and Applications. Elsevier, pp. 1–40. https://doi.org/10.1016/B978-0-444-53348-7.00001-6.

Ashley, G.M., 1990. Classification of large-scale subaqueous bedforms: a new look at an old problem-SEPM bedforms and bedding structures. J. Sediment. Res. 60 (1).

Bagnold, R.A., 1941. 1941: The Physics of Blown Sand and Desert Dunes. Methuen, London.

Baddock, M.C., Nield, J.M., Wiggs, G.F., 2018. Early-stage aeolian protodunes: Bedform development and sand transport dynamics. Earth Surf. Proc. Land. 43 (1), 339–346.

Baitis, E., Kocurek, G., Smith, V., Mohrig, D., Ewing, R.C., Peyret, A.P., 2014. Definition and origin of the dune-field pattern at White Sands, New Mexico. Aeolian Res. 15, 269–287.

Bristow, C.S., 2009. Ground penetrating radar in aeolian dune sands. Ground Penetrating Radar: Theory Appl. 273–297.

Bristow, C.S., Bailey, S.D., Lancaster, N., 2000. The sedimentary structure of linear sand dunes. Nature 406 (6791), 56.

Bristow, C.S., Jol, H.M., Augustinus, P., Wallis, I., 2010. Slipfaceless 'whaleback' dunes in a polar desert, Victoria Valley, Antarctica: insights from ground penetrating radar. Geomorphology 114 (3), 361–372.

Brookfield, M.E., 1977. The origin of bounding surfaces in ancient aeolian sandstones. Sedimentology 24 (3), 303–332.

Brothers, S.C., Kocurek, G., Brothers, T.C., Buynevich, I.V., 2017. Stratigraphic architecture resulting from dune interactions: White Sands Dune Field New Mexico. Sedimentology 64 (3), 686–713.

Chan, M.A., 1989. Erg margin of the Permian white rim sandstone, SE Utah. Sedimentology 36 (2), 235–251.

Chan, M.A., Kocurek, G., 1988. Complexities in eolian and marine interactions: processes and eustatic controls on erg development. Sed. Geol. 56 (1–4), 283–300.

Charru, F., 2006. Selection of the ripple length on a granular bed sheared by a liquid flow. Phys. Fluids 18 (12), 121508.

Clarbout, J.F., 1985. Imaging the Earth's Interior. Blackwell Scientific Publications, Palo Alto, California.

Claudin, P., Andreotti, B., 2006. A scaling law for aeolian dunes on Mars, Venus, Earth, and for subaqueous ripples. Earth Planet. Sci. Lett. 252 (1), 30–44.

Claudin, P., Wiggs, G.F.S., Andreotti, B., 2013. Field evidence for the upwind velocity shift at the crest of low dunes. Bound.-Layer Meteorol. 148 (1), 195–206.

Cooper, W.S., 1958. Coastal sand dunes of Oregon and Washington. Geolog. Soc. Am. Memoirs 72, 1–162.

Durán, O., Claudin, P., Andreotti, B., 2011. On aeolian transport: Grain-scale interactions, dynamical mechanisms and scaling laws. Aeolian Res. 3 (3), 243–270.

Eastwood, E., Nield, J., Baas, A., Kocurek, G., 2011. Modelling controls on aeolian dune-field pattern evolution. Sedimentology 58 (6), 1391–1406.

Elbelrhiti, H., 2012. Initiation and early development of barchan dunes: a case study of the Moroccan Atlantic Sahara desert. Geomorphology 138 (1), 181–188.

Elbelrhiti, H., Claudin, P., Andreotti, B., 2005. Field evidence for surface-wave-induced instability of sand dunes. Nature 437 (7059), 720.

Ewing, R.C., Kocurek, G.A., 2010. Aeolian dune interactions and dune-field pattern formation: White Sands Dune Field, New Mexico. Sedimentology 57 (5), 1199–1219.

Ewing, R.C., Kocurek, G., Lake, L.W., 2006. Pattern analysis of dune-field parameters. Earth Surf. Proc. Land. 31 (9), 1176–1191.

Ewing, R.C., McDonald, G.D., Hayes, A.G., 2015. Multi-spatial analysis of aeolian dune-field patterns. Geomorphology 240, 44–53.

Fenton, L.K., Bishop, J.L., King, S., Lafuente, B., Horgan, B., Bustos, D., Sarrazin, P., 2017. Sedimentary differentiation of aeolian grains at the White Sands National Monument, New Mexico, USA. Aeolian Res. 26, 117–136.

Fourriere, A., Claudin, P., Andreotti, B., 2010. Bedforms in a turbulent stream: formation of ripples by linear linear instability and dunes by nonlinear pattern coarsening. J. Fluid Mech. 649, 287–328.

Fryberger, S.G., 2001. Geological Overview of White Sands National Monument. National Park Service.

Fryberger, S.G., Ahlbrandt, T.S., Andrews, S., 1979. Origin, sedimentary features, and significance of low-angle eolian" sand sheet" deposits, Great Sand Dunes National Monument and vicinity, Colorado. J. Sedimentary Res. 49 (3), 733–746.

Fryberger, S.G., Hesp, P., Hastings, K., 1992. Aeolian granule ripple deposits. Namibia. Sedimentology 39 (2), 319–331.

Gadal, C., Rozier, O., Claudin, P., Courrech Du Pont, S., Narteau, C., 2017, December. Dune growth under multidirectional wind regimes. In: American Geophysical Union, Fall Meeting 2017, abstract #EP41B-1840.

Gao, X., Gadal, C., Rozier, O., Narteau, C., 2018. Morphodynamics of barchan and dome dunes under variable wind regimes. Geology 46 (9), 743–746.

Hersen, P., Douady, S., Andreotti, B., 2002. Relevant length scale of barchan dunes. Phys. Rev. Lett. 89 (26), 264301.

Holm, D.A., 1960. Desert geomorphology in the Arabian Peninsula. Science 132, 1369–1379.

Jackson, P.S., Hunt, J.C.R., 1975. Turbulent wind flow over a low hill. Q. J. Roy. Meteor. Soc. 101 (430), 929–955.

Jerolmack, D.J., Ewing, R.C., Falcini, F., Martin, R.L., Masteller, C., Phillips, C., Reitz, M.D., Buynevich, I., 2012. Internal boundary layer model for the evolution of desert dune fields. Nat. Geosci. 5 (3), 206.

Jerolmack, D.J., Reitz, M.D., Martin, R.L., 2011. Sorting out abrasion in a gypsum dune field. J. Geophys. Res. Earth Surf. 116 (F2).

Jol, H.M. (Ed.), 2009. Ground penetrating radar theory and applications Elsevier.

Jol, H.M., Bristow, C.S., 2003. GPR in sediments: advice on data collection, basic processing and interpretation, a good practice guide. Geolog. Soc., London, Sp. Publ. 211 (1), 9–27.

Jordan, O.D., Mountney, N.P., 2010. Styles of interaction between aeolian, fluvial and shallow marine environments in the Pennsylvanian to Permian lower Cutler beds, south-east Utah, USA. Sedimentology 57 (5), 1357–1385.

Kocurek, G., 1981. Significance of interdune deposits and bounding surfaces in aeolian dune sands. Sedimentology 28 (6), 753–780.

Kocurek, G., 1991. Interpretation of ancient eolian sand dunes. Annu. Rev. Earth Pl. Sc. 19 (1), 43–75.

Kocurek, G., Carr, M., Ewing, R., Havholm, K.G., Nagar, Y.C., Singhvi, A.K., 2007. White Sands Dune Field, New Mexico: age, dune dynamics and recent accumulations. Sed. Geol. 197 (3), 313–331.

Kocurek, G., Ewing, R.C., 2016. Trickle-Down and trickle-up boundary conditions in eolian dune-field pattern formation. In: Budd, D.A., Hajek, E.A., Purkis, S.J. (Eds.),

Autogenic Dynamics and Self-Organization in Sedimentary Systems. SEPM (Society for Sedimentary Geology), Tulsa, Oklahoma, pp. 5–17. https://doi.org/10.2110/sepmsp.106.04.

Kocurek, G., Lancaster, N., 1999. Aeolian system sediment state: theory and Mojave Desert Kelso dune field example. Sedimentology 46 (3), 505–515.

Kocurek, G., Nielson, J., 1986. Conditions favourable for the formation of warm-climate aeolian sand sheets. Sedimentology 33 (6), 795–816.

Kocurek, G., Townsley, M., Yeh, E., Havholm, K., Sweet, M.L., 1992. Dune and dune-field development on Padre Island, Texas, with implications for interdune deposition and water-table-controlled accumulation. J. Sediment. Res. 62 (4).

Kroy, K., Sauermann, G., Herrmann, H.J., 2002. Minimal model for sand dunes. Phys. Rev. Lett. 88 (5), 054301.

Lancaster, N., 1982. Dunes on the Skeleton Coast, Namibia (South West Africa): geomorphology and grain size relationships. Earth Surf. Proc. Land. 7 (6), 575–587.

Lancaster, N., 1996. Field studies of sand patch initiation processes on the northern margin of the Namib sand sea. Earth Surf. Proc. Land. 21 (10), 947–954.

Langford, R.P., 2003. The Holocene history of the White Sands dune field and influences on eolian deflation and playa lakes. Quat. Int. 104 (1), 31–39.

Loope, D.B., 1984. Eolian origin of upper Paleozoic sandstones, southeastern Utah. J. Sediment. Res. 54 (2).

Loope, D.B., 1985. Episodic deposition and preservation of eolian sands: A late Paleozoic example from southeastern Utah. Geology 13 (1), 73–76.

McKee, E.D., 1966. Structures of dunes at White Sands National Monument, New Mexico (and a comparison with structures of dunes from other selected areas). Sedimentology 7 (1), 3–69.

Momiji, H., Nishimori, H., Bishop, S.R., 2002. On the shape and migration speed of a proto-dune. Earth Surf. Proc. Land. 27 (12), 1335–1338.

Mountney, N.P., 2006. Periodic accumulation and destruction of aeolian erg sequences in the Permian Cedar Mesa Sandstone, White Canyon, southern Utah. USA. Sedimentology 53 (4), 789–823.

Neal, A., 2004. Ground-penetrating radar and its use in sedimentology: principles problems and progress. Earth-Sci. Rev. 66, 261–330. https://doi.org/10.1016/j.earscirev.2004.01.004.

Newton, B.T., Allen, B., 2014. Hydrologic Investigation at White Sands National Monument. New Mexico Bureau of Geology and Mineral Resources, Aquifer Mapping Program.

Nield, J.M., Wiggs, G.F., Squirrell, R.S., 2011. Aeolian sand strip mobility and protodune development on a drying beach: examining surface moisture and surface roughness patterns measured by terrestrial laser scanning. Earth Surf. Proc. Land. 36 (4), 513–522.

Nielson, J., Kocurek, G., 1986. Climbing zibars of the Algodones. Sed. Geol. 48 (1–2), 1–15.

Pedersen, A., Kocurek, G., Mohrig, D., Smith, V., 2015. Dune deformation in a multidirectional wind regime: White Sands Dune Field, New Mexico. Earth Surf. Proc. Land. 40 (7), 925–941.

Ping, L., Narteau, C., Dong, Z., Zhang, Z., Du Pont, S.C., 2014. Emergence of oblique dunes in a landscape-scale experiment. Nat. Geosci. 7 (2), 99.

Porter, M.L., 1986. Sedimentary record of erg migration. Geology 14 (6), 497–500.

Rachal, D.M., Dugas, D.P., 2009. Historical dune pattern dynamics: White Sands dune field, New Mexico. Phys. Geography 30 (1), 64–78.

Richards, K.J., 1980. The formation of ripples and dunes on an erodible bed. J. Fluid Mech. 99 (3), 597–618.

Rubin, D.M., 1987. Cross-bedding, bedforms and paleocurrents. Society of Economic Paleontologists and Mineralogists, Oklahoma (EUA).

Rubin, D.M., Hunter, R.E., 1982. Bedform climbing in theory and nature. Sedimentology 29 (1), 121–138.

Sauermann, G., Kroy, K., Herrmann, H.J., 2001. Continuum saltation model for sand dunes. Phys. Rev. E 64 (3), 031305.

Seager, W.R., Morgan, P., 1979. Rio Grande rift in southern New Mexico, west Texas, and northern Chihuahua. Rio Grande rift: Tectonics and magmatism 87–106.

Seager, W., Hawley, J., Kottlowski, F.E., Kelley, S.A., 1987. Geology of the East Half of the Las Cruces and Northeast El Paso 2-Degree Sheets Southern New Mexico. New Mexico Bureau of Mines and Mineral Resources, Socorro.

Smith, J.D., 1970. Stability of a sand bed subjected to a shear flow of low Froude number. J. Geophys. Res. 75 (30), 5928–5940.

Swanson, T., Mohrig, D., Kocurek, G., 2016. Aeolian dune sediment flux variability over an annual cycle of wind. Sedimentology 63 (6), 1753–1764.

Szynkiewicz, A., Ewing, R.C., Moore, C.H., Glamoclija, M., Bustos, D., Pratt, L.M., 2010. Origin of terrestrial gypsum dunes—implications for martian gypsum-rich dunes of Olympia Undae. Geomorphology 121 (1), 69–83.

Warren, A., 1971. Dunes in the Tenere desert. Geogr. J. 458–461.

Wilson, I.G., 1973. Ergs. Sedimentary Geol. 10 (2), 77–106.

Yilmaz, Ö., 2001. Seismic data analysis. Soc. Exploration Geophys. https://doi.org/10.1190/1.9781560801580.

Young, K.F., Frederikse, H.P.R., 1973. Compilation of the static dielectric constant of inorganic solids. J. Phys. Chem. Ref. Data 2 (2), 313–410.